ACS APPLIED MATERIALS & INTERFACES

www.acsami.org Research Article

Photo-Cross-Linked and Photothermal *Flammulina velutipes* Polysaccharide Hydrogel Loaded with Caffeic Acid-Copper Nanozyme for Diabetic Wound Healing

Meimei Fu,[¶] Qianru Xiang,[¶] Zhuoyi Huang,[¶] Wenjun Luo, Zhou Fang, Jintao Li, Yue Li, Zijun Xia, Yangjia Huang, Yitao Zhao, Wenzhen Liao,[*] and Jinshan Guo[*]

Cite This: *ACS Appl. Mater. Interfaces* 2025, 17, 53145−53167 Read Online

ACCESS | Metrics & More | Article Recommendations | Supporting Information

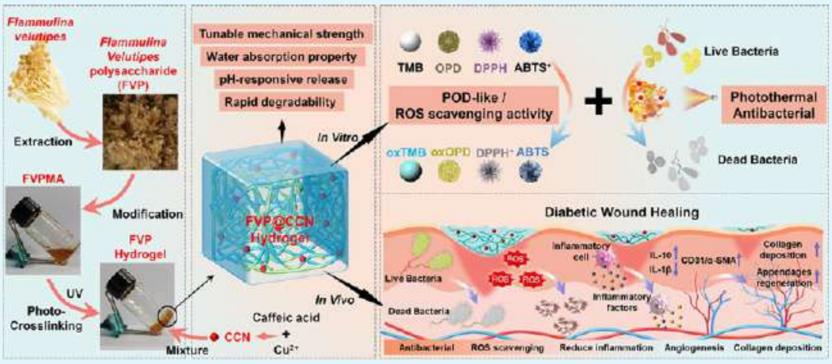

ABSTRACT: Diabetic ulcers remain a persistent global health challenge. Developing therapeutic systems with antibacterial, antioxidant, anti-inflammatory, and pro-angiogenic properties presents a promising strategy for effectively and rapidly treating diabetic wounds and preventing the development of diabetic ulcers. Herein, a photo-cross-linked *Flammulina velutipes* polysaccharide (FVP) containing double bonds was obtained through extraction and purification of FVP, and a facile reaction using methacrylic anhydride. The FVP was further combined with caffeic acid-copper nanozyme (CCN) to fabricate a series of multifunctional photo-cross-linked hydrogels (FVP@CCN) for diabetic wound healing. The FVP@CCN demonstrated rapid degradability, tunable mechanical properties, considerable intrinsic antimicrobial activity, and excellent biocompatibility. Additionally, the incorporated CCN, possessing peroxidase-like nanozyme activity, further endowed FVP@CCN with strong photothermal-induced antimicrobial ability, reactive oxygen species (ROS) scavenging capability, angiogenesis promotion activities, and pH-responsive release of CA and Cu^{2+}. In vivo studies confirmed that FVP@CCN provided synergistic treatment against multiple healing impairments associated with diabetic wounds, exhibiting hemostasis, sustainable antibacterial, antioxidant, anti-inflammatory, angiogenesis-promotion, cell-proliferation, and hair follicle-regeneration, ultimately resulting in a diabetic wound closure rate exceeding 90% within 7 days. The multifunctional FVP@CCN hydrogel holds significant potential for diabetic wound healing, and its fabrication strategy can be extended to other plant-based polysaccharide hydrogels.

KEYWORDS: *Flammulina velutipes polysaccharide (FVP), caffeic acid, copper, nanozyme, diabetic wound healing*

1. INTRODUCTION

Diabetes is a highly prevalent chronic metabolic disorder, affecting 537 million adults aged 20−79 worldwide in 2021, a figure projected to rise to 783 million by 2045, according to The IDF Diabetes Atlas 10 the edition.[1,2] If left untreated or inadequately managed, the intricate pathophysiological mechanisms underlying diabetic wounds frequently culminate in the development of diabetic foot ulcers (DFUs).[3] The estimated lifetime risk for diabetic patients to develop DFUs is as high as 34%, accompanied by a 5 year mortality rate of 30.5%.[4,5] In the United States, this imposes a substantial burden by straining both patient well-being and healthcare resources, resulting in over 70,000 lower extremity amputations and medical expenditures exceeding $25 billion annually.[6] The failure of diabetic wounds to undergo timely and effective healing is primarily due to a significantly elevated risk of bacterial infection, severe oxidative stress, persistent inflammatory responses, and inadequate angiogenesis.[7,8] The hyperglycemic

Received: June 11, 2025
Revised: August 26, 2025
Accepted: September 11, 2025
Published: September 15, 2025

https://doi.org/10.1021/acsami.5c11453
ACS Appl. Mater. Interfaces 2025, 17, 53145−53167

Scheme 1. Schematic Diagram Depicting the Fabrication and Underlying Mechanism of the FVP@CCN Hydrogel for Accelerating Diabetic Wound Healing[a]

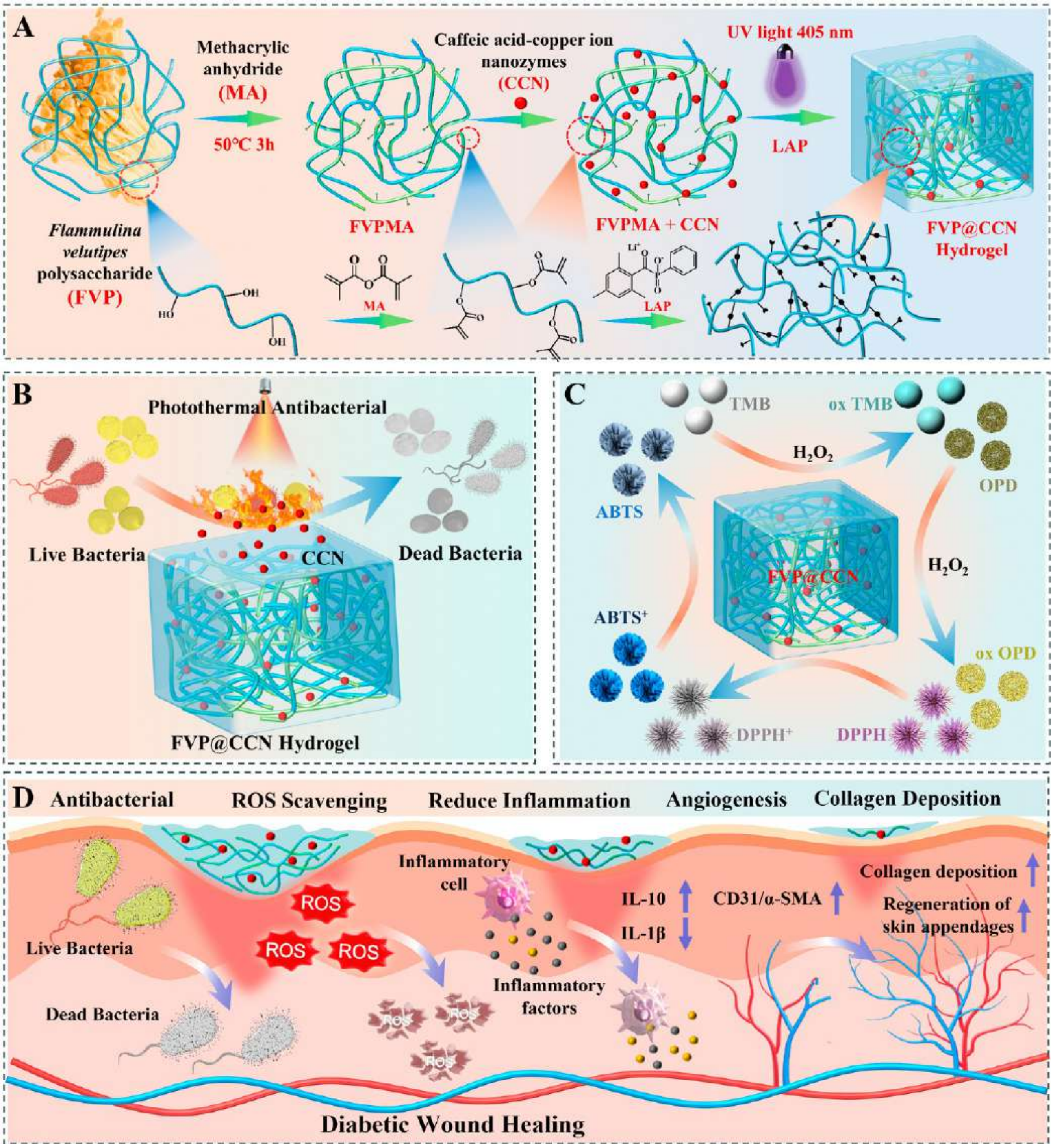

[a] (A) Design strategy and fabrication of *F. velutipes* polysaccharides (FVP) hydrogel loaded with caffeic acid-copper ion nanozymes (CCN). (B) Antibacterial mechanism of FVP@CCN hydrogel. (C) The schematic illustration of ROS scavenging capacity and POD-like nanozyme activity of FVP@CCN hydrogels. (D) Multimodal therapeutic effects promoting scarless healing through: (i) antimicrobial action; (ii) inflammation modulation; (iii) vascularization enhancement; and (iv) collagen remodeling.

environment exacerbates bacterial proliferation and ROS generation, leading to sustained oxidative stress that perpetuates inflammation and microvascular dysfunction.[9,10] Traditional therapies for nonhealing diabetic wounds, such as decompression therapy, surgical debridement, negative pressure wound therapy, and antibiotic therapy, while effective to some extent, are often limited by suboptimal therapeutic outcomes and associated side effects.[11,12] For instance, the ubiquitous employment of antibacterial agents has led to an increase in bacterial resistance, while the instability of anti-

https://doi.org/10.1021/acsami.5c11453
ACS Appl. Mater. Interfaces 2025, 17, 53145−53167

inflammatory medications further restricts their long-term efficacy. Consequently, developing innovative strategies to address chronic diabetic wounds, particularly integrated therapies targeting their multiple pathologic mechanisms, is urgently needed.

In recent years, significant advancements within regenerative medicine have provided novel therapeutic prospects for diabetic wounds.[13,14] Evidence indicates that the diabetic wounds healing process can be significantly improved through effective management of bacterial infections,[15] eliminating reactive oxygen species (ROS),[16] modulating the inflammatory microenvironment within wounds,[17] promoting angiogenesis,[18,19] regulating macrophage phenotype and quantity,[20,21] as well as inhibiting extracellular matrix (ECM) degradation.[22,23] However, single-approach interventions fail to fully address the complex challenges of diabetic wound healing.[24,25] Therefore, multifunctional biomaterials combining antimicrobial, antioxidant, anti-inflammatory, and pro-angiogenic properties, particularly microenvironment-targeting materials, represent a breakthrough strategy.

Hydrogels, as an emerging wound dressing material, have attracted considerable interest owing to their ECM-like structure, exceptional biocompatibility, and continuous moisturizing ability.[26,27] Formed by the cross-linking of hydrophilic polymer chains, hydrogels maintain stability during debridement and provide a conducive moist microenvironment for wounds to promote tissue repair and regeneration.[28] In addition, hydrogels can serve as an ideal platform for localized drug delivery or as platforms for photothermal/photodynamic therapy (PTT/PDT),[29,30] and can incorporate bioactive compounds or cellular elements.[31,32] Notably, the wound microenvironment undergoes dynamic changes throughout the repair process.[33] In diabetic wounds particularly, these dynamic changes are often accompanied by alterations in pH, growth factors, and cytokine profiles. Hydrogels with microenvironment-responsive properties enable on-demand drug release and environmentally sensitive biodegradation in response to such changes.[34,35] Therefore, the development of multifunctional hydrogels that not only dynamically modulates the wound microenvironment, but also enables responsive on-demand drug release and allows for adjustable degradation rates, provides a promising approach for enhancing diabetic wound healing.[36] However, selecting hydrogels with excellent biocompatibility, versatile tunable properties, and the capacity to directly enhance diabetic wound healing while also serving as a responsive drug delivery platform has remained a significant challenge within the context of the diabetic wound microenvironment.[37]

Therefore, natural polysaccharide materials are a potential option due to their rich sources, renewability, and excellent bioactivity.[38,39] In particular, polysaccharides derived from fungi exhibit significant potential in the preparation of hydrogels for wound dressing applications due to their batch-to-batch consistency, high cost-effectiveness, and significant biological activity.[40,41] *Flammulina velutipes* (*F. velutipes*, FV), globally recognized as the fourth most popular edible mushroom, primarily comprises polysaccharides and glycoproteins as its bioactive constituents.[42] The *F. velutipes* polysaccharides (FVP) have been reported to exhibit a spectrum of beneficial biological activities, such as antimicrobial, anti-inflammatory, immunomodulatory, antitumor, and antiaging properties.[43] Studies have demonstrated that the application of modified FVP-based wound materials can significantly expedite the wound healing process and stimulate hair follicle regeneration.[44,45] Hair follicle regeneration is often considered a sign that the skin regeneration process is approaching the restoration of normal tissue structure and function,[46] suggesting FVP's potential in promoting scarless healing. However, relying solely on the therapeutic effects of FVP may prove inadequate for achieving significant healing outcomes for diabetic wounds. Therefore, to overcome the limitations of monotherapy, copper-based phenolic metal−organic framework (MOF) nanozyme technology from our previous research work was introduced to endow the hydrogel with photothermal capabilities while augmenting its antioxidant and antibacterial functions.[47−49]

Herein, we developed a multifunctional hydrogel dressing with efficient responsiveness, incorporating a therapeutic system with antimicrobial, antioxidant, anti-inflammatory, and pro-angiogenic properties for rapid healing of diabetic wounds (Scheme 1). The multifunctional hydrogels (FVP@CCN) were synthesized through: (1) extraction and purification of FVP; (2) methacrylation modification; and (3) photoinitiated polymerization with copper-caffeinate nanozymes (CCN) (Scheme 1A). The in situ forming FVP@CCN hydrogel exhibits appropriate mechanical strength, effectively providing physical wound coverage while protecting against external environmental damage. Its rapid degradation properties facilitate painless dressing changes, thereby maximizing its potential for promoting wound healing at all times. Meanwhile, the combination of the intrinsic antimicrobial effect of FVP and the photothermal bactericidal effect of CCN, together with the responsive dissociation and release of caffeic acid and copper ions under the acidic pH conditions of diabetic wounds, collectively contributes to a synergistic antimicrobial effect that inhibits the development of wound infections (Scheme 1B). FVP@CCN hydrogel not only inherits the multiple bioactivities of FVP but also enhances its physical therapeutic ability by loading CCN, which includes the ability to effectively scavenge excessive hydrogen peroxide at the wound site through the peroxidase-like activity of CCN, regulating oxidative stress (Scheme 1C). As expected, we successfully established a protective barrier on diabetic mouse wounds through direct local injection of FVP@CCN and subsequent photopolymerization. The results demonstrated that the FVP@CCN hydrogel continuously and intelligently modulated the wound microenvironment throughout different stages of healing, thereby promoting the healing process of diabetic wounds (Scheme 1D). In summary, the FVP@CCN hydrogel represents an advanced therapeutic concept that challenges traditional diabetic wound management limitations. By combining polysaccharide's biocompatibility with copper-based phenolic nanozyme's multifunctionality, the FVP@CCN hydrogel provides a novel solution to effectively address chronic diabetic wound therapeutic challenges, demonstrating broad clinical application prospects.

2. MATERIALS AND METHODS

2.1. Materials. *F. velutipes* were harvested from the untamed mountainous forests of Fujian Province, China. Methacrylic anhydride (MA, CAS 760-93-0) and the Sephadex G-100 column were purchased from Aladdin Biological Technology Co., Ltd. (Shanghai, China). Caffeic acid (CA, CAS 331-39-5) and $CuSO_4{\cdot}5H_2O$ (CAS 7758-99-8) were procured from Macklin Biochemical Technology Co., Ltd. (Shanghai, China). Lithium phenyl-2,4,6-trimethylbenzoylphosphinate (LAP, CAS 85073-19-4) was purchased from SunP Biotech Co., Ltd. (Beijing, China). The DEAE Cellulose-52 column was acquired from Dingguo Biotechnology Co., Ltd. (Beijing, China). Monosaccharide standards, including L-fucose, rhamnose, etc., were supplied by Bo Rui Saccharide Biotech Co., Ltd. (Yangzhou, China). All chemicals were used without further purification.

2.2. Synthesis of CCN. Caffeic acid (CA, 0.5 g) was solubilized in 30 mL of distilled water, followed by pH adjustment to 8.0 using an ammonia solution (28 wt %). $CuSO_4 \cdot 5H_2O$ (0.5 g dissolved in 10 mL distilled water) was added gradually to the alkaline CA solution to give a flocculent precipitation. After being agitated for 10 min, the mixture solution was centrifuged at 6000 rpm for 10 min. The obtained precipitate was extensively washed with deionized water and lyophilized for 24 h to acquire the caffeic acid-copper ion nanozymes (CACu nanozyme, CCN). The morphological characteristics of CCN were examined by scanning electron microscopy (SEM, Quanta 200, Japan). The Fourier transform infrared (FTIR) spectrum profile of CCN was additionally acquired using an infrared spectrometer (Thermo Scientific, Nicolet-iS10). The crystallinity and element compositions of CCN were also characterized by high-resolution transmission scanning electron microscopy (HRTEM, JEOL JEM-F200), Raman spectrometer (Horiba LabRam Confocal Raman), X-ray diffraction (XRD, Bruker D8), and X-ray photoelectron spectroscopy (XPS, Thermo Fisher Scientific, Escalab 250Xi), respectively.

2.3. Extraction, Purification, and Identification of Polysaccharides from *F. velutipes*. *F. velutipes* (FV) was initially freeze-dried using a Scientz-10N lyophilizer (Ningbo, China) and ground into a fine powder. The resulting powder was mixed with distilled water and subjected to hot water extraction under heating, after which the solution was filtered to remove insoluble residues. The retained solids underwent reflux extraction with 80% (v/v) ethanol at 80 °C for 1 h. Subsequently, a second round of extraction and filtration was performed with distilled water. The combined filtrate was concentrated using a rotary evaporator at 70 °C, after which four volumes of prechilled anhydrous ethanol were introduced, and the mixture was stored at 4 °C overnight. Deproteinization was carried out using a combination of trypsin and sevage reagent. The solution was dialyzed against distilled water to remove inorganic salts, low-molecular-weight impurities, and pigments. Then, three volumes of anhydrous ethanol were incorporated, and the mixture was again held at 4 °C overnight. The precipitated polysaccharides were washed twice with anhydrous ethanol and lyophilized to constant weight. Finally, centrifugation was performed at 12,000 rpm to collect the crude polysaccharides as the precipitate.[50]

The crude polysaccharide obtained from centrifugation was dissolved in distilled water at a concentration of 50 mg/mL by heating. The resulting solution was fractionated on a DEAE cellulose-52 column (2.6 cm × 50 cm), with elution carried out using distilled water followed by NaCl solution (0.1 mol/L) with a 1.0 mL/min flow rate. Elution solution was collected at 10 min intervals in equal volumes, and the polysaccharide content was determined by the phenol-sulfuric acid method. An elution profile was constructed with the eluent tube number represented on the *x*-axis and the absorbance measured at 490 nm on the *y*-axis. The single eluting peak was collected and lyophilized. The same procedure was repeated for further purification using a Sephadex G-100 column (2.6 cm × 50 cm). The major peak fraction was again collected, lyophilized, and denoted as FVP for subsequent structural characterization and bioactivity evaluation.

The monosaccharide constituents of FVP were determined by an ion chromatograph (Thermo Fisher, USA) employing a Dionex Carbopac PA20 column. 5 mg of FVP was hydrolyzed with 2 mL of 3 M trifluoroacetic acid (TFA) at 120 °C for 3 h. After hydrolysis, the solution was carefully transferred to a nitrogen-purged tube and evaporated to dryness. The residue was reconstituted in 5 mL of deionized water and vortex-mixed thoroughly. An aliquot of 50 μL was then diluted with 950 μL of deionized water and centrifuged at 12,000 rpm for 5 min. The resulting supernatant was collected for ion-exchange chromatography (IC) analysis. The same protocol was applied for the analysis of monosaccharide standards.

The Fourier transform infrared (FTIR) spectrum of FVP was also recorded by an infrared spectrometer (Thermo Scientific, Nicolet-iS10, USA). The NMR spectral data for FVP1 were acquired on a Bruker Avance III 600 MHz spectrometer maintained at 25 °C. Spectral processing and interpretation were performed using MestRe Nova software (version 5.3.0, Mestrelab Research S.L.). The morphology of FVP was observed by a stereoscopic microscope (Shunyu, SZN71, China) and scanning electron microscopy (SEM, Quanta 200, Japan).

2.4. Synthesis of FVPMA. FVP (0.5 g) was dissolved in 10 mL of carbonate-bicarbonate buffer (0.25 M) at 55 °C. Under a stirring condition, 2 mL MA was infused at a flow rate of 0.5 mL/min. After reacting for 3 h at 55 °C with stirring, the solution was dialyzed (1000 Da molecular weight cut-off (MWCO)) with deionized water at room temperature for 5 days. The resulting FVPMA product was then lyophilized for subsequent use. The content of carbon−carbon double bonds (n(C═C)) before and after modification was determined by the iodometric method. Additionally, the hydroxyl content in FVP was determined by acid−base titration, and the substitution rate of carbon−carbon double bonds was subsequently calculated. The FVPMA polymers were characterized by ^{1}H NMR (400 MHz, Bruker Ascend 400 MHz NMR instrument) and FTIR spectrometer.

2.5. Preparation of FVP@CCN Hydrogel and Characterizations. First, 1 mL FVPMA (5%, w/v) was mixed with 2.5 μL LAP initiator (0.25%, w/v). Different proportions of CCN were added to the FVPMA solution containing LAP and thoroughly mixed. Notably, before addition, the CCN samples were subjected to extensive grinding and ultrasonic dispersion to minimize aggregation. Then FVP@CCN was synthesized via cross-linking induced by 405 nm ultraviolet irradiation for 5 min. According to the volume of FVPMA solution, CCN was added at 50 μg/mL, 100 μg/mL, 200 μg/mL, 500 μg/mL, and 1000 μg/mL to obtain five FVP@CCN hydrogels, and they were named FVP@CCN$_{0.05}$, FVP@CCN$_{0.1}$, FVP@CCN$_{0.2}$, FVP@CCN$_{0.5}$, and FVP@CCN$_1$, respectively. FVP hydrogels without adding CCN were prepared as a control using the same procedures.

The structural features and elemental composition of the FVP@CCN hydrogels were characterized using a field emission scanning electron microscope (ZEISS SIGMA) coupled with an energy-dispersive X-ray spectroscopy (EDS) detector. The FTIR spectra of FVP, CCN, and representative FVP@CCN were recorded with an infrared spectrometer (Thermo Scientific, Nicolet-iS10). The swelling ratios of FVP@CCN were measured by the mass difference of the dried FVP@CCN hydrogels (W_d) before and after being immersed in water until a swelling equilibrium (W_s) was reached. The swelling ratio was determined according to the formula below: swelling (%) = $(W_s - W_d) \times 100\%/W_d$. At least five parallels were established, and the mean value was calculated from the results.

The degradation profiles of FVP@CCN hydrogels were studied by measuring the mass losses at preset time points of the dried hydrogels. The initial weight (W_i) was recorded in PBS (0.01 M, pH 7.4) at 37 °C, respectively. At the preset time points, the sample was collected, washed with deionized water, and freeze-dried to obtain the weight (W_t). The mass loss was determined according to the formula: mass loss (%) = $(W_i - W_t) / W_t \times 100\%$. At least 5 parallels were established, and the mean value was calculated from the results.

The pH-responsive release of CA was also studied by immersing FVP@CCN hydrogel in PBS solution (0.1 M) with different pH values (6, 7.4, and 8.5) at 37 °C. At designated time points (12, 24, 48, 60, 72, 96, 120 h), the concentration of released CA was determined by UV−vis spectrophotometer (Shimadzu, UV-2600).

The mechanical properties of FVP@CCN hydrogels were evaluated through compression testing using a tensile testing machine (Instron 34TM-10) equipped with a 50 N load cell. The sample was made into a cylinder (diameter × height, 8 mm × 10 mm) for compression testing at a constant rate of 5 mm/min until compressed to 80% strain. At least 5 parallels for each composite hydrogel were established, and the mean value was calculated from the results. The compressive modulus was derived from the slope of the initial linear region (0−10%) of the stress−strain curve.

The degree of cross-linking of FVP@CCN hydrogels was assessed by mechanical properties. The cross-linking density was derived based on the Young's modulus of the FVP@CCN hydrogel, which was obtained from the corresponding stress−strain curves. The effective cross-linking density (V) of the hydrogels was determined by the following formula: $G \approx RTV\phi^{(1/3)}$, where R represents the gas constant (8.3144 J/(mol K)), ϕ represents the volume fraction of solvent molecules in the hydrogel network, and T represents the absolute temperature (K). The cross-linking density (V) was calculated to be 0.57 mol/m^3. It should be noted that cross-linking density is influenced by many factors, and its value will change due to the changes of the concentration of enzyme, cross-linking agent, and the experimental temperature, among other variables.[51]

2.6. Nanoenzyme Activity. *2.6.1. DPPH Radical Scavenging Activity.* In brief, a freeze-dried FVP@CCN hydrogel film (3 mg) was introduced into 2,2-diphenyl-1-picrylhydrazyl (DPPH) solution (4 mL, 100 μM) in methanol. After incubation in the dark for a preset time, the absorbance of the DPPH solution at 517 nm (A_s) was determined with a UV−vis spectrophotometer. The corresponding value of the untreated DPPH solution (A_b) served as the blank reference. The DPPH scavenging percentage was determined according to the formula below: DPPH scavenging (%) = $(A_b - A_s)/A_b \times 100\%$.[49]

2.6.2. ABTS⁺ Radical Scavenging Activity. The $ABTS^+$ working solution was prepared by mixing 7.4 mM 2,2′-azinobis-(3-ethylbenzthiazoline-6-sulphonate) (ABTS) and 2.6 mM $K_2S_2O_8$ solutions and allowing the mixture to react for 12 h in the dark. Subsequently, the $ABTS^+$ radical working solution was diluted with 0.01 M PBS solutions until the absorbance at 734 nm reached 0.8 ± 0.02 (A_s). Subsequently, 3 mg of freeze-dried FVP@CCN hydrogel film was added, and the reaction was conducted in the dark for a specified period. The $ABTS^+$ radical scavenging rate was then determined at a wavelength of 734 nm (A_b). The $ABTS^+$ scavenging rate was calculated using the following equation: $ABTS^+$ scavenging (%) = $(A_b - A_s)/A_b \times 100\%$.[52]

2.6.3. Evaluation of POD-Enzyme-like Activity. The peroxidase-like activity of FVP@CCN was assessed by measuring its capacity to catalyze the oxidation of 3,3′,5,5′-tetramethylbenzidine (TMB) to oxTMB in the presence of H_2O_2. Briefly, FVP@CCN was added to 1 mL PBS solution (pH 4.0) supplemented with H_2O_2 (20.0 μL, 0.5 M) and TMB (20.0 μL, 16.0 mM) to initiate the catalytic process. The kinetics of the reaction were assessed by recording the absorbance of oxTMB at 652 nm using a UV−vis spectrophotometer at specific time intervals. Furthermore, the peroxidase-like activity of FVP@CCN was further characterized using OPD, and the product 2,3-diaminophenazine (DAP) was measured for its UV−vis absorbance at 450 nm using a method similar to that employed for TMB.[53]

2.7. Photothermal Property and Antibacterial Experiment *In Vitro*. *2.7.1. Photothermal Property.* To evaluate the photothermal response, the FVP@CCN hydrogel was exposed to irradiation using an 808 nm near-infrared laser (B0T808-5W) at 2.0 W/cm^2. Variations in temperature were monitored and recorded by a near-infrared (NIR) thermal imaging system (UTI260B). Subsequently, we observed the temperature changes of $FVP@CCN_{0.5}$ (as a representative FVP@CCN hydrogel) under different laser powers (1.0, 2.0, and 3.0 W/cm^2). To assess the reproducible photothermal performance and operational stability of FVP@CCN, four consecutive heating−cooling cycles were conducted. Thermal imaging and temperature profiles under light irradiation were captured using a near-infrared (NIR) thermal camera.

2.7.2. Antibacterial Experiment. Antibacterial experiment: the antibacterial efficacy of FVP@CCN hydrogels was assessed *in vitro* against *Escherichia coli*, *Staphylococcus aureus*, and methicillin-resistant *S. aureus* (MRSA) both in the presence and absence of near-infrared (NIR) light irradiation. Briefly, a bacterial suspension with 10^7 CFUs/mL was combined with the FVP@CCN hydrogels and incubated at 37 °C for 24 h. Subsequently, the bacterial suspension was analyzed using both spread and drop plate methods, followed by an additional 24 h incubation period at 37 °C to facilitate colony observation and quantification. In addition, bacterial suspension (10 μL, 10^8 CFUs/mL) was applied to the surface of FVP@CCN hydrogels and subsequently irradiated with an 808 nm NIR laser (2.0 W/cm^2) for 10 min. Bacterial suspension (10^8 CFUs/mL, 10 μL) in 200 μL of PBS served as the negative control and was similarly subjected to NIR laser irradiation (808 nm, 2.0 W/cm^2). After all samples were exposed to bacteria ± NIR irradiation for 10 min, sterile PBS (1 mL) was introduced to resuspend the surviving bacteria. Then, the diluted bacterial suspensions (100 μL) were uniformly plate on TSA agar and cultured at 37 °C for 24 h, followed by CFU counting. All experimental procedures were conducted in triplicate, and the mean value was calculated from the results.

2.8. Biocompatibility of the Hydrogels *In Vitro*. Mouse fibroblasts (L929) and human umbilical vein endothelial cells (HUVECs) were incubated in complete DMEM containing 1% penicillin/streptomycin and 10% FBS. Cells were cultured in a humidified incubator (Thermo Fisher Scientific, USA) at 37 °C and 5% CO_2.

2.8.1. Cytotoxicity Evaluation. The potential cell toxicity of FVP@CCN hydrogels on L929 cells and HUVECs was assessed using the extraction solution of FVP@CCN using the CCK-8 assay. For preparation of extraction solution, dried FVP@CCN hydrogels (0.5 g) were incubated in PBS (5 mL, pH 7.4) at 37 °C for 24 h, and the collected supernatant was neutralized to pH 7.4, sterilized via filtration through a 0.2 μm filter, to obtain the extraction solution. Both 0.1 mL L929 and HUVECs cell suspension (4×10^4 cells/mL) were seeded into 96-well plate and incubated under standard culture conditions to promote cell adhesion. Subsequently, the cells were incubated for 24 h in complete DMEM with a 10% (v/v) extract solution. Following medium aspiration, CCK-8 reagent was added to each well and incubated under 5% CO_2 for 2 h. The optical density (OD) was then determined by measuring absorbance at 450 nm. Cells cultured in complete DMEM alone served as the control group. The cell viabilities were calculated according to the formula below: cell viability (%) = $(A_b - A_s)/(A_c - A_s) \times 100\%$. A_b denotes the OD value of the sample at 450 nm, A_c represents the OD value of the control at the same wavelength, and A_s represents the OD value of the 10% CCK-8 solution.

2.8.2. Cell Proliferation Evaluation. The proliferation activity of FVP@CCN hydrogels on L929 cells was assessed via Live/Dead staining and CCK-8 assay using the extraction solution of FVP@CCN. L929 cells (5×10^3 cells/well) were seeded in a 96-well plate and incubated under standard culture conditions to promote cell adhesion. L929 Cells were subsequently cultured in complete DMEM containing 10% (v/v) extract solution for 1, 3, and 5 days. Then, using a CCK-8 kit to determine the OD value at a specific point in time. Meanwhile, Live/Dead staining solution (Bestbio, China) was used to mark the cell status. Cell morphology and proliferation were monitored using an inverted fluorescence microscope (Olympus CKX41, Tokyo, Japan). At least three parallels were set for each group, and the quantitative results were averaged.

2.8.3. Scratch Assay Experiment. The influence of FVP@CCN hydrogels on cell migration was assessed via a scratch assay. The L929 cells (5×10^5 cells/mL) were seeded in a 6-well plate. Following a 24 h incubation in complete DMEM to facilitate cell adhesion and monolayer establishment, three linear scratches were generated with a 1 mL pipet tip. The floating cells were then removed by washing three times with sterile PBS (pH 7.4), and the remaining cells were cultured in complete DMEM containing the extraction solution of FVP@CCN for 12 and 24 h. Following 12 and 24 h incubation periods, scratch images were captured using an inverted fluorescence microscope. Tests of each group were repeated three times. The migration rate was calculated with ImageJ software according to the formula: Migration rate (%) = $(W_i - W_t)/W_i \times 100\%$, where W_i indicates the initial scratch width at 0 h, W_t denotes the scratch width after t hours (t = 12 or 24) of culture.

2.8.4. Transwell Experiment. The L929 cells were used for transwell experiment to obtain the OD value of cell migration. Transwell chambers (Corning, 353097) were placed in 24-well plates containing DMEM and the extraction solution of FVP@CCN. L929 cells (1×10^4 cells/mL) were seeded into the upper chambers (200

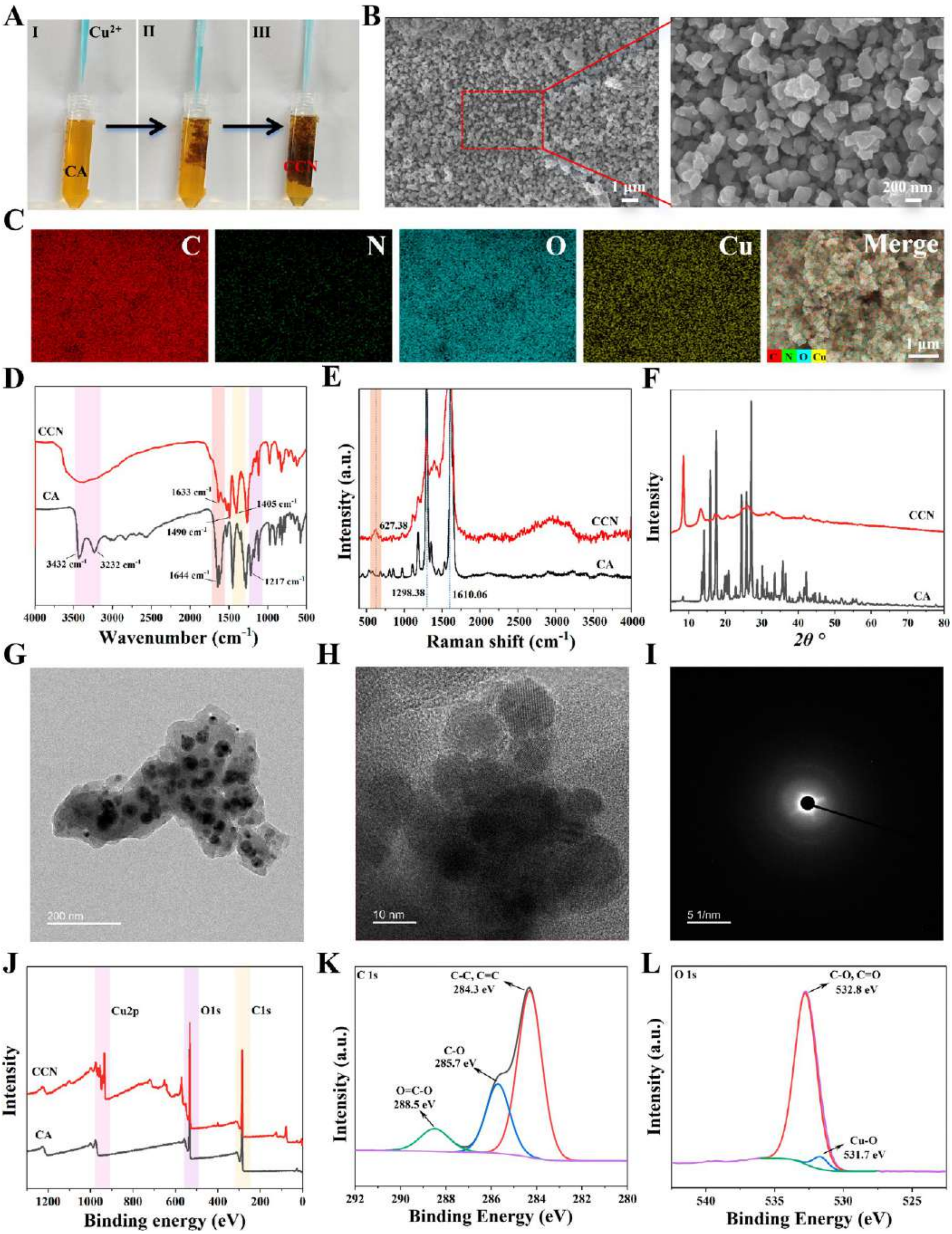

Figure 1. Characterizations of CACu nanozyme (CCN). (A) Images of CCN synthesis process. (B) SEM image of CCN. (C) EDS mapping analysis revealed the element distribution in CCN. (D) FTIR spectra of CA and CCN. (E) Raman spectra of the CA and CCN. (F) XRD patterns

Figure 1. continued

of CA and CCN. HRTEM images at (G) the 200 nm scale and (H) the 10 nm scale. (I) SAED pattern of CCN. (J) XPS spectra of CA and CCN. The high-resolution (K) C 1s and (L) O 1s XPS spectra of CCN.

μL/chamber) and incubated for 24 h. Cells on the upper membrane surface were completely removed with a cotton swab. Migrated cells on the lower surface were fixed with 4% paraformaldehyde for 15 min, stained with crystal violet for 15 min, rinsed with PBS, and imaged under a microscope. The chamber was then immersed in 33% glacial acetic acid to elute the stain, and the absorbance of the eluate was measured at 570 nm.

2.8.5. In Vitro Tube Formation Assay. The angiogenic potential of FVP@CCN was evaluated using an *in vitro* endothelial tube formation assay. Matrigel matrix glue (Corning, 356234) was added to a 96-well plates at 50 μL per well, followed by the plate in an incubator 37 °C incubator for over 1 h. Then HUVECs (2×10^4 cells/mL) were added to the plate containing matrix glue and incubated for 6 h. AO/EB staining was performed to label the cells, and tube formation was visualized by fluorescence microscopy. The extent of tube formation was quantified using ImageJ software. Tests were repeated three times, and for each group at least 3 parallels were set.

2.8.6. The Intracellular Reactive Oxygen Species Assay. The antioxidant capacity of FVP@CCN in L929 cells was assessed using a reactive oxygen species (ROS) assay kit. L929 cells were seeded in 24-well plates (8000 cells/well) and incubated at 37 °C for 24 h in complete DMEM containing the extraction solution of FVP@CCN. After incubation, the cells were incubated with 2,7-dichlorodihydrofluorescein diacetate (DCFH-DA) solution for 20 min. Cellular fluorescence was subsequently analyzed with an inverted fluorescence microscope. Rosup-treated cells served as the positive control, while untreated cells were used as the negative control.

2.9. The Hemostatic Capacity of FVP@CCN Hydrogel.

Male Sprague−Dawley rats (~ 300 g) were used to assess hemostatic efficacy by both tail amputation and liver incision models. The animals were randomly allocated into three groups ($n = 3$ for each group): control, FVP hydrogel, and FVP@CCN hydrogel groups. Following intraperitoneal anesthesia with sodium pentobarbital (2% w/v, 50 mg/kg), the rats were immobilized on a surgical platform. In the tail amputation model, complete transection was performed at the 10th caudal vertebra, followed by immediate application of the hydrogel precursor solution and UV-induced gelation at the amputated site. For the liver incision model, a midline laparotomy was performed to expose the liver. After removing surface exudate, a standardized wound (3 mm depth × 7 mm length) was created on the left lobe using a microsurgical blade. The hydrogel precursor solution was immediately administered and photopolymerized under UV light to form a gel covering the bleeding site. For both models, preweighed filter paper was used to absorb hemorrhagic exudate until active bleeding ceased. The filter paper was then reweighed to determine total blood loss through weight differential measurements.

2.10. *In Vivo* Diabetes Wound Regeneration Evaluation of the FVP@CCN Hydrogels.

Male C57BL/6 mice (6 weeks, 22.5 ± 2.5 g) were purchased from the Experimental Animal Center of Southern Medical University, and the gender of the mice had no effect on the experimental results. Throughout the experimental period, mice were housed in group cages to minimize stress levels and facilitate natural behavioral expression and social interactions. All animal studies were approved by the Animal Experimental Committee of Institute of Biological and Medical Engineering, Guangdong Academy of Sciences (Approval No. 2021011) and conducted in accordance with Chinese Guidelines for the Ethical Use of Experimental Animals and the ARRIVE guidelines. To induce type 1 diabetes, fasted C57BL/6 mice received intravenous streptozotocin (STZ; 70 mg/kg) in sterile citrate buffer (0.05 mol/L sodium citrate, pH 4.5) for five consecutive days. Diabetes was confirmed by measuring blood glucose levels every 3 days until consistent hyperglycemia (>16.7 mmol/L) was maintained for 30 days.

The diabetes wound regeneration potential of the FVP@CCN hydrogels was evaluated *in vivo* using full-thickness wound models on diabetic C57BL/6 mice. The mice were randomly assigned to 4 groups ($n = 5$): Control, FVP hydrogels (FVP), FVP@CCN hydrogels (FVP@CCN), and FVP@CCN hydrogels with 808 nm NIR for 10 min (FVP@CCN + NIR). It is noteworthy that FVP@$CCN_{0.5}$ was ultimately selected as the wound intervention material for diabetic mice based on comprehensive evaluations of physical properties, antioxidant capacity, antibacterial performance, and biologically validated cellular activities across hydrogel formulations with varying composition ratios of FVP and CCN. All animals were anesthetized via intraperitoneal administration of chloral hydrate (0.3 mg/kg) with isoflurane as an adjunct to anesthesia, and the dorsal fur was shaved using an electric clipper and completely removed with depilatory cream to fully expose the surgical area. A full-thickness skin wound was generated on the depilated area using an 8 mm biopsy punch. Following standard disinfection procedures, the wound and surrounding skin were rinsed and sterilized with sterile saline and iodophor, respectively. Then, FVP and FVP@CCN hydrogels were administered to the wounds, while the control group was left untreated with only basic cleaning and disinfection. For the FVP@CCN + NIR group, the wounds covered with FVP@CCN hydrogel received additional 808 nm NIR irradiation for 10 min. Notably, 808 nm NIR photothermal therapy was performed daily until the FVP@CCN was completely absorbed. Wound healing was photographically documented on days 0, 1, 3, 5, 7, 10, and 14 postinjury. Wound areas were quantified using ImageJ software.

2.10.1. Histological Analysis. Wound samples were collected for histopathological examination to assess re-epithelialization, collagen deposition, inflammatory infiltration, and neovascularization. Briefly, on postoperative days 3, 7, and 14, some animals were sacrificed, and the wound tissues were collected. The wound tissues were fixed with 4% paraformaldehyde overnight, dehydrated, embedded in paraffin, and finally cut into 4 μm slices. Then the embedded tissue slices were used for histological hematoxylin−eosin (H&E) and Masson's trichrome staining, interleukin-1β (IL-1β) and interleukin-10 (IL-10) immunohistochemistry, and CD31/α-SMA immunofluorescence staining, observed and recorded under a fluorescence microscope (Leica DM4000 B, Wetzlar, Germany) to examine re-epithelialization, collagen formation, inflammatory response, and angiogenesis within the wound tissue. The biosafety of the FVP@CCN hydrogel was evaluated through H&E staining of major organs, including the heart, liver, spleen, lung, and kidney, on day 14 post-treatment.

2.11. *In Vivo* Antimicrobial Validation of FVP@CCN Hydrogels.

Male STZ-induced diabetic mice (10 weeks) were used to establish an infected wound model. The mice were randomly assigned to four groups ($n = 6$ per group): (1) control group, (2) FVP hydrogel (FVP), (3) FVP@CCN hydrogel (FVP@CCN), and (4) FVP@CCN hydrogel with near-infrared irradiation (FVP@CCN + NIR). After anesthesia, the dorsal hair was shaved and sterilized, followed by the creation of full-thickness skin wounds using an 8 mm biopsy punch. A logarithmic-phase *S. aureus* suspension (20 μL, 1×10^7 CFUs/mL) was evenly inoculated onto the wound surface and covered with a sterile dressing for 24 h to ensure bacterial colonization. Then the wounds were treated according to the designed protocols. On day 3 post-treatment, wound tissues were harvested for bacterial plate counting (to quantify bacterial load) and Gram staining (to assess infection severity).

2.12. Statistical Analysis.

All the experimental data were statistically analyzed and presented as mean ± standard deviation (SD). Differences between groups were assessed by *t*-test or one-way ANOVA. A *p*-value of less than 0.05 was considered statistically significant. *, **, and *** represent $p < 0.05$, $p < 0.01$, and $p < 0.001$, respectively.

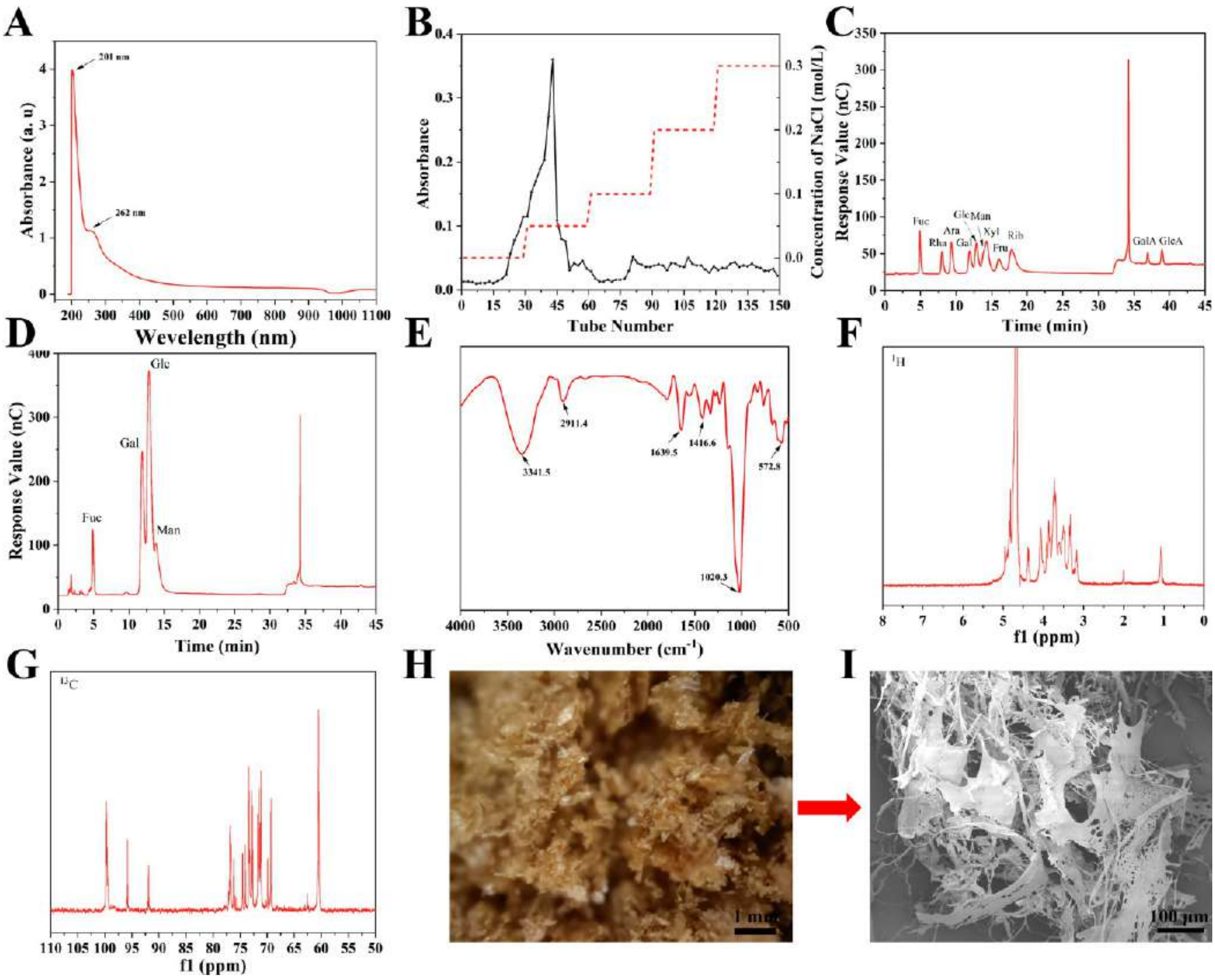

Figure 2. Extraction, purification, and identification of polysaccharides from *F. velutipes*. (A) Ultraviolet spectrum scanning of crude polysaccharides. (B) Elution profile of the crude polysaccharides on DEAE-cellulose-52 column. (C) Ion chromatograms of standard 16 monosaccharides. (D) Ion chromatograms of FVP. (E) FT-IR, (F) ^{1}H NMR and (G) ^{13}C NMR spectra of FVP. (H) Optical bright-filled images and (I) SEM images of FVP.

3. RESULTS AND DISCUSSION

3.1. Synthesis of CCN. CCN was synthesized via coordination between copper ions and the ortho-phenolic hydroxyl groups of caffeic acid at room temperature under alkaline conditions (Figures 1A and S1). The elevated reaction pH (8.0) facilitated the deprotonation of catechol moieties, while an increased Cu^{2+} concentration promoted the establishment of a Cu−CA coordination architecture. The morphological features, structural characteristics, and elemental composition of CCN were analyzed using SEM coupled with EDS mapping (Figure 1B,C). SEM revealed CCN formed microparticles averaging 200 nm (Figures 1B and S2), with EDS mapping confirming uniform Cu^{2+} coordination with CA (Figure 1C). In addition, the coordination between Cu^{2+} and CA was also confirmed by FT-IR, Raman spectra, XRD, HRTEM, and XPS (Figure 1D−L). The FT-IR spectrum of CA exhibited characteristic absorption bands at 1644 cm^{-1} (C═O stretch), 1217 cm^{-1} (C−O stretch of phenolic OH), and broad bands around 3432 cm^{-1} and 3232 cm^{-1} (O−H stretching vibrations). These peaks were substantially attenuated or absent in the spectrum of CCN, indicating successful coordination and structural integration.[54,55] Moreover, the FT-IR spectrum of CCN displayed new bands characteristic of carboxylate anion vibrations, including symmetric COO^- stretches at 1405 and 1490 cm^{-1}. A slight redshift was also observed in the carbonyl (C═O) stretching vibration, which shifted from 1644 cm^{-1} to 1633 cm^{-1} (Figure 1D).[18,56] Furthermore, comparative analysis of Raman spectra for CA and CCN showed a characteristic peak at 627.38 cm^{-1} in CCN, which is attributed to Cu−O vibration resulting from phenolic hydroxyl−Cu^{II} interaction (Figure 1E).[57] The XRD pattern showed sharp crystalline peaks, suggesting the presence of a crystalline structure in CCN (Figure 1F). The crystalline structure of CCN was conclusively verified through HRTEM and selected area electron diffraction (SAED) characterizations (Figure 1G−I). HRTEM images (Figure 1G,H) demonstrate that CCN samples exhibited agglomerated morphology at 200 nm scale, while clearly defined particle boundaries and distinct lattice fringes with a *d*-spacing of 0.363 nm were clearly resolved at 10 nm scale. The corresponding SAED pattern (Figure 1I) displays characteristic polycrystalline diffraction

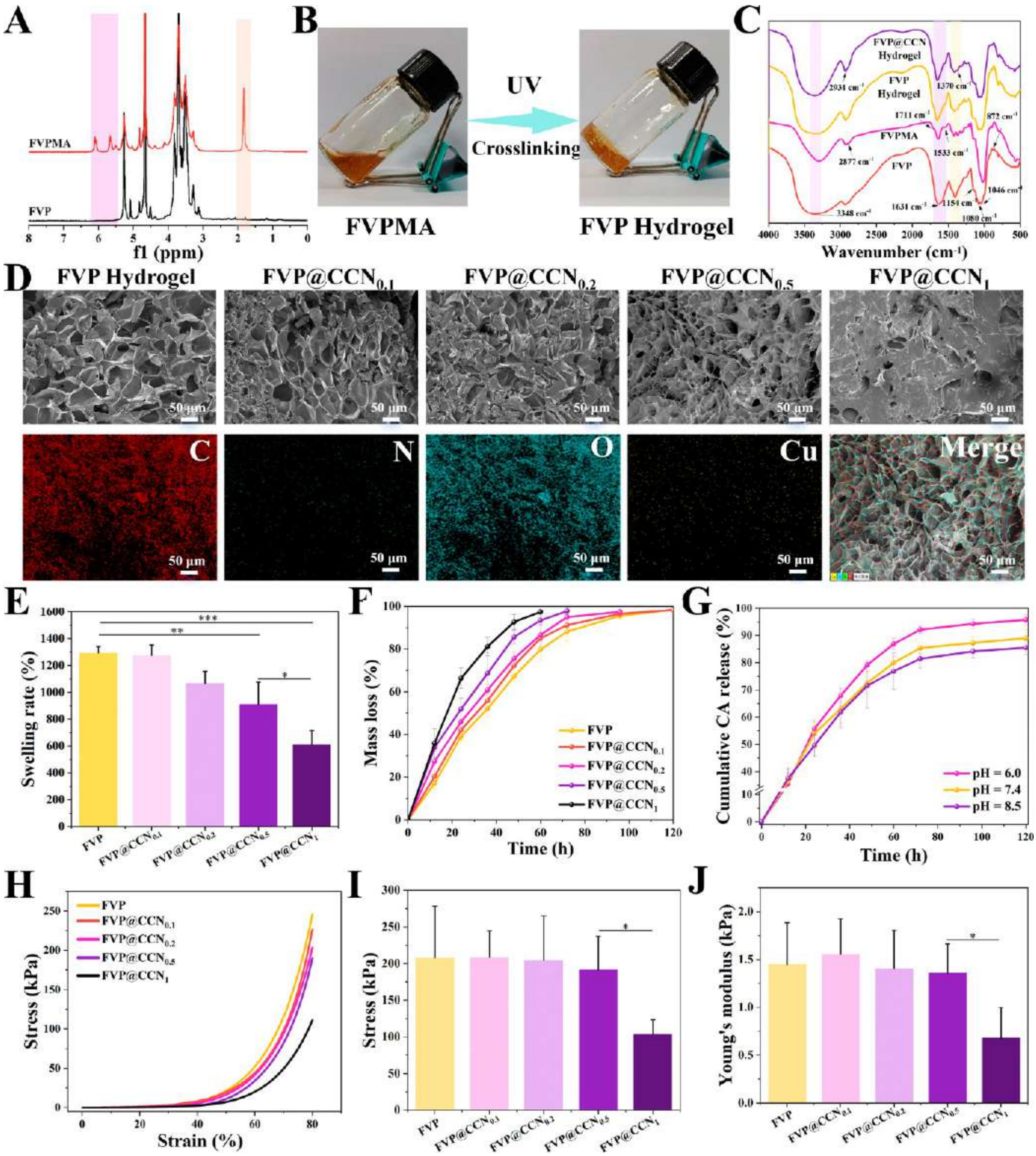

Figure 3. Preparation and characterization of FVP@CCN hydrogels. (A) ^{1}H NMR to verify the presence of methacryloxy groups in FVPMA. (B) The gelation behavior of FVP@CCN hydrogel. (C) FT-IR of FVP, FVPMA, FVP hydrogel, and FVP@CCN hydrogel. (D) SEM images of FVP@CCN hydrogels prepared with different proportions of FVP and CCN, and SEM−EDS elemental mapping of FVP@CCN$_{0.5}$ (magnification: 200×). (E) Swelling ratios of FVP@CCN Hydrogels (n = 5). (F) Degradation profiles of FVP@CCN hydrogels (n = 5). (G) The cumulative concentrations of CA in solutions with different pH values (n = 5). (H) Representative stress−strain curves. (I) Compression strengths (n = 5). (J) Young's modulus of different FVP@CCN hydrogel formulations (n = 5). *$p < 0.05$, **$p < 0.01$, and ***$p < 0.001$.

rings that are consistent with the XRD data, collectively confirming the crystalline nature of CCN. In addition, the valence state of Cu in CCN was confirmed by XPS, and the characteristic peaks located at 935 eV were assigned to the Cu 2p, along with the satellite peaks, confirmed the successful incorporation of Cu (Figure 1J).[58] The high-resolution C 1s spectrum exhibited three distinct peaks at approximately 284.3 eV (C−C, C═C), 285.7 eV (C−O), and 288.5 eV (O−C═O) (Figure 1K). The O 1s spectrum displayed two peaks at 531.7 eV (Cu−O) and 532.8 eV (C−O, C═O) (Figure 1L), confirming the successful formation of coordination bonds in CCN.[59]

3.2. Extraction, Purification, and Identification of *Flammulina velutipes* Polysaccharide. The crude polysaccharides were extracted from *F. velutipes* and subjected to hot water extraction to obtain a water-soluble polysaccharide fraction. Following deproteinization, 3.45 g of purified FVP was obtained from 100 g of lyophilized fruiting body powder, corresponding to a yield of 3.45% (w/w). UV−vis spectrophotometric analysis (Figure 2A) revealed a peak at 201 nm, indicating relatively high purity. The crude polysaccharides were fractionated on a DEAE sepharose fast flow column eluted with distilled water and a gradient of NaCl solution. Following anion-exchange chromatography using a DEAE-sepharose column, a distinct elution peak was detected, achieving effective fractionation of the crude polysaccharides into a purified fraction, designated as FVP (Figure 2B). The carbohydrate and protein contents of crude polysaccharides and relatively pure FVP were determined using the phenol-sulfuric acid method and the bicinchoninic acid (BCA) assay. The results in Table S1 indicated that the carbohydrate mass ratio content of crude polysaccharide was 77.36%, and the protein mass ratio was 11.09%. After further chromatographic purification, the carbohydrate content of FVP was 98.57%, and the protein mass ratio was 0, suggesting that our extracted FVP had a very high purity and protein impurities were within the allowable range.

The monosaccharide composition of FVP was determined by ion chromatography. Precisely configured concentrations of each monosaccharide standard solution served as the standard mixture. Quantification was performed using an absolute calibration method, and molar ratios were calculated based on the determined masses and corresponding molecular weights of each monosaccharide. As shown in Table S2, FVP was mainly composed of fucose (7.51%), galactose (29.63%), glucose (41.28%) and mannose (21.58%). The primary monosaccharide constituents of FVP comprised galactose, glucose, and mannose, suggesting that the principal chain of FVP is primarily composed of galactose, glucose, and mannose residues. The corresponding ion chromatograms are presented in Figure 2C,D.

The FVP was analyzed using FT-IR spectroscopy within the 500−4000 cm^{-1} range (Figure 2E), identifying key functional groups and chemical bonds. The spectrum displayed a broad, intense peak at 3341.5 cm^{-1}, corresponding to hydroxyl stretching vibrations, along with a weaker signal at 2911.4 cm^{-1} indicative of C−H stretching vibration. The absorption band near 1639.5 cm^{-1} suggested hydrogen-bonded water molecules. Furthermore, the peak at approximately 1416.6 cm^{-1} was assigned to carbonyl groups, while the signal at 1020.3 cm^{-1} specifically confirmed glycosidic bond presence.

The ^1H and ^{13}C NMR spectra of FVP revealed characteristic signals corresponding to glycosidic linkages, monosaccharides, and chemical shifts (Figure 2F,G). The glycosidic linkage configuration of FVP was determined through ^1H NMR analysis, showing characteristic α-form glucose signals between 4.67 and 4.38 ppm. Additionally, the signal characteristics of carbohydrates were observed in the 3.15−4.06 ppm region (Figure 2F). In the ^{13}C NMR spectrum, the anomeric carbon region (90.0−110.0 ppm) exhibited signals corresponding to L-mannose, L-arabinose, L-rhamnose, D-glucose, and D-galactose. The resonance at 99.64 ppm was attributed to the anomeric carbon of both terminal and internal α-(1 → 2)-linked D-mannopyranosyl residues. The signal at 95.90 ppm indicated the C-1 α of L-arabinose, while the signal at 92.09 ppm corresponded to C1 of α-D-galactose. The carbohydrate-specific signals were further confirmed by peaks in the 60.41−77.11 ppm range (Figure 2G). The morphological characteristics of the FVP were carefully observed. As shown in Figure 2H,I, the FVP showed a brown flocculent morphology, and this unique appearance characteristic may be closely related to its complex molecular structure and aggregation state.

3.3. Characterizations of FVP@CCN Hydrogel. Multifunctional wound dressings are preferred owing to the inherent complexities associated with diabetic wound healing process.[37] A bioengineered multifunctional hydrogel derived from *F. velutipes* polysaccharides and integrated with metal-phenol nanozymes was developed using an optimized protocol to facilitate the healing of diabetic wounds (Scheme 1). First, FVP was reacted with MA under specific conditions to produce FVPMA. As shown in Figure 3A, the structure of FVP and FVPMA were confirmed by ^1H NMR, which revealed the presence of characteristic peaks at 5.6 and 6.2 ppm indicative of the methacryloxy groups.[60] Additionally, the characteristic resonance peak of the methyl group at 1.8 ppm emerged following the incorporation of MA. The substitution rate of the methacryloyl group in FVPMA was calculated as 46.37%.[61,62] Furthermore, the formation of FVP@CCN hydrogel was observed after the addition of the photoinitiator of LAP to the FVPMA + CCN solution and subsequent exposure to 405 nm UV light irradiation (Figure 3B), confirming successful FVPMA synthesis. Simultaneously, the structures of unmodified FVP, FVPMA, FVP hydrogel, and the FVP hydrogel loaded with CCN (FVP@CCN) were characterized using FTIR (Figure 3C). The broad absorption at 3300−3500 cm^{-1} corresponds to O−H stretching vibrations, while peaks at 2931 and 2877 cm^{-1} were associated with the asymmetric stretching vibrations of $-CH_2$ groups. The characteristic peak for amide I was observed at 1631 cm^{-1}, and typical polysaccharide structure absorption peaks appear at 1154, 1080, 1046, and 872 cm^{-1}. Compared to the unmodified FVP, the characteristic peaks of amide I at 1631 cm^{-1} in both FVPMA and FVP hydrogel exhibited a shift. Additionally, new absorption peaks for FVPMA appeared at 1711, 1533, and 1370 cm^{-1}, which were weakened or disappeared in FVP hydrogel and FVP@CCN.[44,45] This indicated that the reaction introduced methacryloyl substituents onto FVP, and subsequently, under LAP and UV irradiation, the unsaturated double bonds polymerized and cross-linked to form the hydrogel. The microscopic morphology of the FVP@CCN hydrogels was observed using SEM. As shown in Figure 3D, the fabricated hydrogel exhibited porous architecture. However, with the increasing concentration of CCN, the pore size of the hydrogel gradually diminished, and the structure began to become disordered, which may be attributed to the catechol groups present in CCN affecting the polymerization and cross-linking of unsaturated double bonds.[63,64] Additionally, EDS demonstrated that Cu^{2+} were uniformly distributed throughout the hydrogel in small quantities, indicating that the CCN nanoparticles were homogeneously dispersed within the FVP hydrogel matrix (Figure 3D).

3.4. Swelling, Degradation, and pH-Responsive Release, Mechanical Properties of FVP@CCN Hydrogel. Hydrogel dressings are widely recognized for their capacity to absorb wound exudate and sustain a moist microenvironment

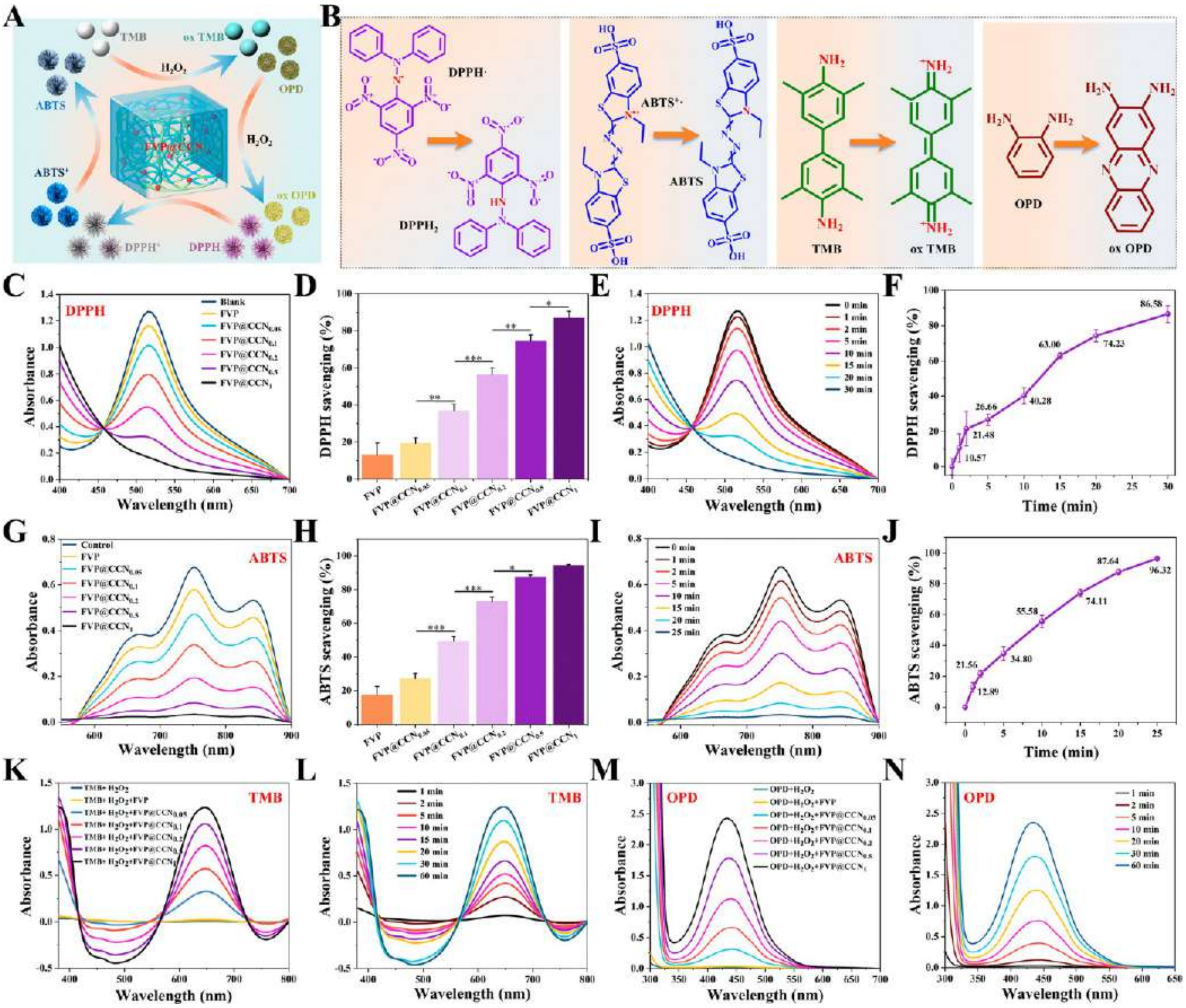

Figure 4. FVP@CCN hydrogels exhibited nanozyme activity, showing exceptional antioxidant capacity. (A) The schematic illustration of the free radical scavenging capacity and POD-like nanozyme activity detection. (B) The schematic illustration of the reduction reaction of DPPH, $ABTS^+$, TMB, and OPD. (C) UV−vis spectra and (D) DPPH radical scavenging rates in 20 min ($n = 3$). (E) UV−vis curves and (F) Time-dependent DPPH scavenging rates of $FVP@CCN_{0.5}$ ($n = 3$). (G) UV−vis spectra and (H) $ABTS^+$ scavenging rates in 20 min ($n = 3$). (I) UV−vis curves and (J) Time-dependent $ABTS^+$ scavenging rates of $FVP@CCN_{0.5}$ ($n = 3$). (K) TMB reactions at different compositions of reaction systems. (L) Time-course of TMB oxidation by $FVP@CCN_{0.5}$. (M) OPD reactions at different compositions of reaction systems. (N) Time-course of OPD oxidation by $FVP@CCN_{0.5}$. $^*p < 0.05$, $^{**}p < 0.01$, and $^{***}p < 0.001$.

that promotes tissue regeneration.[27] Therefore, the swelling ratio of FVP@CCN was evaluated in PBS solution at 37 °C to evaluate its water absorption properties. As shown in Figure 3E, the FVP@CCN hydrogel exhibited favorable water absorption properties, which can be ascribed to its microporous architecture and the abundance of hydrophilic functional groups in the polymeric network. However, with an increased concentration of CCN, the degree of cross-linking in the hydrogel decreased, leading to a reduction in water retention capacity. Furthermore, the biodegradability of materials represents a critical property for biomedical applications. Therefore, the degradation behavior of the FVP@CCN hydrogel series was assessed using PBS solution (pH 7.4) as the degradation medium. Degradation profiles in Figure 3F demonstrated complete mass loss within 7 days for all FVP@CCN formulations, with rates inversely proportional to cross-linking density. Among them, FVP hydrogel exhibited the slowest degradation with the highest cross-linking density. In contrast, $FVP@CCN_1$ with the lowest cross-linking density was almost completely degraded within 3 days. The rapid degradability of FVP@CCN hydrogel offers dual therapeutic advantages for diabetic wound healing. First, it significantly reduces dressing change frequency, thereby eliminating mechanical stripping damage to nascent epithelial tissues during hydrogel removal and preventing secondary wound injury associated with dressing replacement. Second, during the wound healing process, the FVP@CCN hydrogel continuously releases and replenishes fresh active components (Cu^{2+}, CA, and FVP), enabling multitarget modulation of the wound microenvironment to effectively address characteristic pathological features of diabetic wounds. Under alkaline conditions, the phenolic hydroxyl groups in polyphenol molecules readily undergo deprotonation to form oxygen anions (Ph−O$^-$), which efficiently coordinate with metal ions (e.g., Fe^{3+}, Cu^{2+}) to form stable chelate complexes.[57,65] In contrast, under acidic conditions, the high concentration of H^+ disrupts the metal-polyphenol coordination structure through two primary mechanisms: direct competition with metal ions for coordination sites that reduces effective coordination concentration, and protonation of phenolic hydroxyl groups (−O$^-$ → −OH) that significantly diminishes their coordination capacity. These effects ultimately prevent the formation or promote the cleavage of metal-polyphenol coordination bonds, leading to destabilization or dissociation of the chelate structure.[66,67] The pH-responsive release performance of FVP@CCN hydrogels was evaluated by monitoring the release of CA at different pH levels. As shown in Figure 3G, the results indicate that the release of CA occurs more rapidly and substantially at pH 6.5 compared to pH 7.4 and 8.0. Since the pH value of diabetic wounds typically falls below 6.5, FVP@CCN hydrogels with pH-responsive phenolic acid/metal ion release could serve as a potential dressing for diabetic wounds.

The suitable elasticity and mechanical robustness of the material facilitate cutaneous wound repair by preserving structural integrity during tissue deformation under external stress. The stress−strain behavior and Young's modulus of the FVP@CCN hydrogel were assessed (Figure 3H−J). The results indicate that as the CCN content increased, the compressive strength and Young's modulus of the hydrogel decreased. This finding is consistent with previous results, confirming that the mechanical property reduction results from decreased cross-linking density. Furthermore, these results demonstrate that the mechanical properties of the FVP@CCN hydrogels can be modulated by adjusting the CCN content, allowing them to be tailored for different application scenarios. Additionally, Young's modulus of the FVP@CCN hydrogel was used to approximately calculate the cross-linking density,[51,68] and the cross-linking density of $FVP@CCN_{0.5}$, as the representative hydrogel of FVP@CCN hydrogel, is calculated to be 0.57 mol/m^3. Note that cross-linking density is influenced by many factors, and its value will change due to the changes of the concentration of enzyme, cross-linking agent, and the experimental temperature, and other variables.

In summary, the FVP@CCN hydrogel series, characterized by high porosity, excellent water absorption, rapid degradation, pH-responsive release behavior, and tunable mechanical strength, demonstrates significant potential as a quality dressing for diabetic wounds.

3.5. Nanoenzyme Activity of FVP@CCN Hydrogel.

When the skin barrier is compromised, damaged tissues and cells surrounding the wound generate excessive ROS. Excessive ROS in the wound site triggers inflammatory responses that inhibit tissue repair and damage normal cells, establishing a ROS-amplifying vicious cycle.[69] Thus, eliminating excess ROS is essential for promoting diabetic wound healing. The antioxidant capacity and peroxidase-like activity of the FVP@CCN hydrogel were systematically evaluated by using the DPPH, ABTS, TMB, and OPD reagents in relevant experiments (Figure 4A).

DPPH, a stable nitrogen-centered radical, shows purple color in ethanol with characteristic absorption at 517 nm, enabling quantitative assessment of radical scavenging activity (Figure 4B). As shown in Figure 4C,D, FVP hydrogel demonstrated limited radical scavenging activity, scavenging only 18% DPPH within 20 min. The incorporation of CCN significantly improved the DPPH radical scavenging activity in a concentration-dependent manner. Within 20 min, the DPPH scavenging rates of $FVP@CCN_{0.05}$, $FVP@CCN_{0.1}$, $FVP@CCN_{0.2}$, $FVP@CCN_{0.5}$, and $FVP@CCN_1$ were 19.2%, 36.9%, 56.4%, 74.3%, and 86.8%, respectively. After 30 min, the DPPH solution for the $FVP@CCN_{0.5}$ group was completely decolorized with no absorbance peak at 517 nm, indicating that the DPPH radical was almost completely eliminated by $FVP@CCN_{0.5}$ within 30 min (Figure 4E,F).

ABTS could be oxidized to form a stable nitrogen-centered radical ($ABTS^+$), producing a green-blue solution with characteristic absorption at 734 nm (Figure 4B). As shown in Figure 4G,H, similar to the results of DPPH, FVP hydrogel showed weak ABTS free radical scavenging ability. Similarly, the scavenging ability of FVP@CCN for ABTS free radical exhibited CCN concentration-dependent. Within 20 min, the ABTS scavenging rate for $FVP@CCN_{0.05}$ (lowest CCN content) had no significant change with a rate of only 26.9%. In contrast, the ABTS scavenging rates of $FVP@CCN_{0.1}$, $FVP@CCN_{0.2}$, $FVP@CCN_{0.5}$, and $FVP@CCN_1$ significantly increased to 49.2%, 72.7%, 87.4%, and 94.3%, respectively. The characteristic peak at 734 nm in the $FVP@CCN_1$ group nearly disappeared, and the ABTS solution had almost completely decolorized. Notably, $FVP@CCN_{0.5}$ matched $FVP@CCN_1$'s scavenging efficacy by 30 min (Figure 4I,J). These results demonstrate that FVP@CCN possesses excellent antioxidant capacity, making it a competitive candidate for eliminating excess ROS and promoting diabetic wound healing.

Additionally, the POD-like activity of FVP@CCN was spectrally evaluated using TMB and H_2O_2 as substrates (Figure 4K−L). The incubation of H_2O_2 with FVP@CCN generated hydroxyl radicals ($^\bullet OH$), which oxidized TMB to form ox-TMB, producing a characteristic 652 nm peak (Figure 4B). In the UV−vis absorption spectra of the TMB + H_2O_2 group and the TMB + H_2O_2+FVP group, no absorption peak was observed at 652 nm, whereas all groups with TMB + H_2O_2 + FVP@CCN exhibited a characteristic peak at 652 nm, indicating that FVP@CCN possesses peroxidase-like activity. Furthermore, this activity showed CCN concentration-dependent catalytic behavior (Figure 4K). Time-dependent catalytic activity was also investigated (Figure 4L). $FVP@CCN_{0.5}$ showed a time-dependent increase in peak intensity at 652 nm, confirming time-dependent catalytic activity. Furthermore, the peroxidase-like activity was additionally evaluated using *o*-Phenylenediamine (OPD) and H_2O_2 (Figure 4M,N). Under the action of peroxidase, OPD was oxidized by H_2O_2 to polymerize into 2,2′-diaminoazobenzene (DAB) (Figure 4B). The assessment of FVP@CCN's peroxidase-like catalytic activity through the OPD reaction yielded results similar to those observed in the TMB experiment. Specifically, with increased reaction time and CCN concentration, the absorbance peak of FVP@CCN at 450 nm intensified, further confirming the time- and concentration-dependence of CCN of its peroxidase-like activity (Figure 4M,N). Collectively, the behavior of FVP@CCN in both the TMB and OPD reactions demonstrates that the CCN within FVP@CCN hydrogel exhibited catalytic activity analogous to that of peroxidases, suggesting its potential for scavenging excess hydrogen peroxide and alleviating oxidative stress.

3.6. Photothermal Performance and Antibacterial Experiment of FVP@CCN Hydrogel *In Vitro*.

The heightened sensitivity of subcutaneous tissue to bacterial

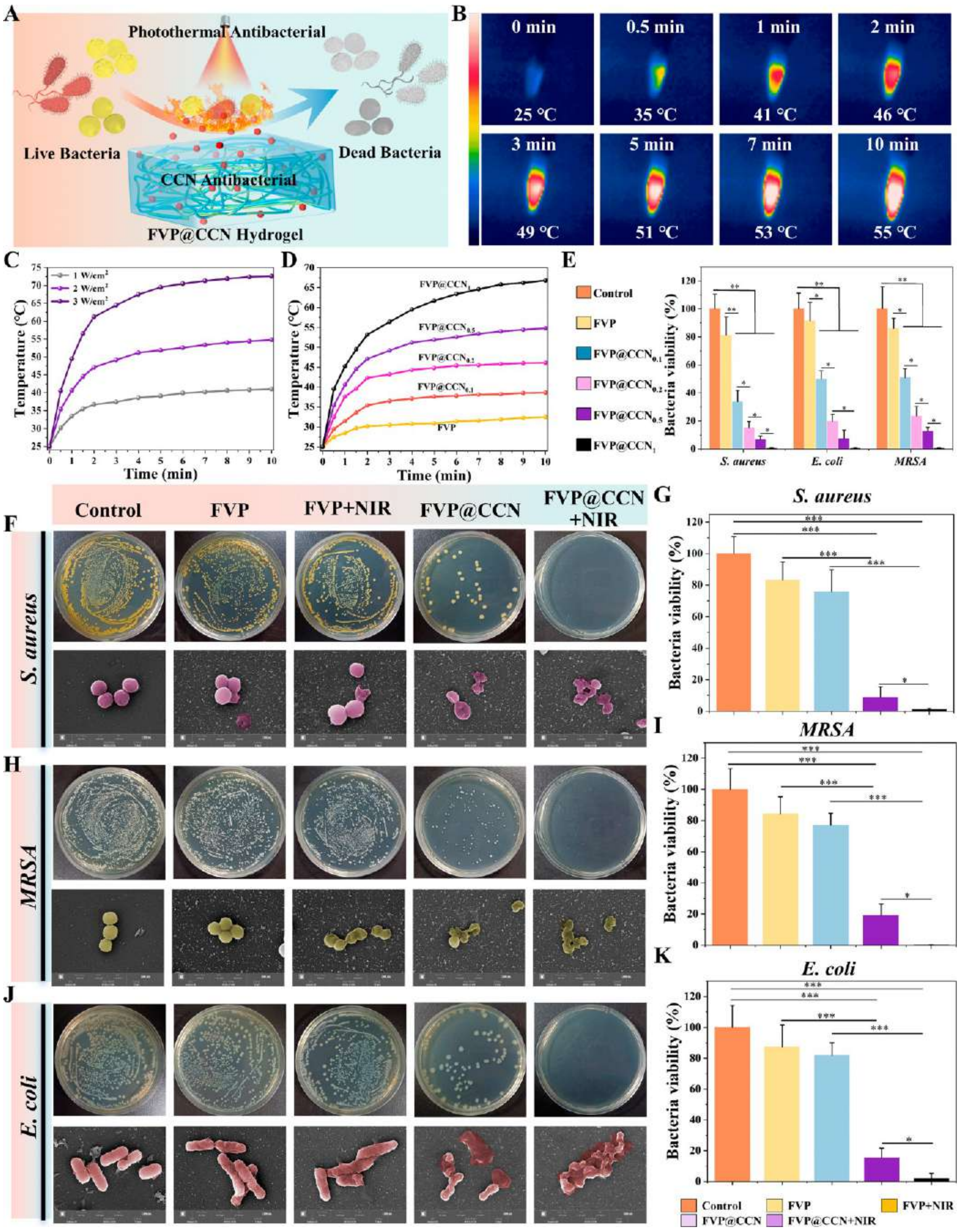

Figure 5. FVP@CCN hydrogels exhibited significant photothermal properties and demonstrated potent *in vitro* antibacterial efficacy. (A) The schematic illustration of the antibacterial mechanism of FVP@CCN hydrogel. (B) Thermographic images of FVP@CCN$_{0.5}$ under NIR irradiation at 2.0 W/cm^2. (C) The temperature-NIR irradiation time curves for FVP@CCN$_{0.5}$ at 1.0, 2.0, and 3.0 W/cm^2. (D) The temperature-NIR irradiation time curves for FVP@CCN hydrogels at 2.0 W/cm^2. (E) The statistical map of bacterial survival for different FVP@CCN hydrogels (*n*

Figure 5. continued

= 3). The images and the SEM images of (F) *S. aureus*, (H) *MRSA*, and (J) *E. coli*. The corresponding bacterial survival quantitative results of (G) *S. aureus*, (I) *MRSA*, and (K) *E. coli* ($n = 3$). $^{*}p < 0.05$, $^{**}p < 0.01$, $^{***}p < 0.001$.

infiltration emphasizes the necessity for wound dressings to possess strong antibacterial properties.[70] Given FVP@CCN's inherent antimicrobial activity and known photothermal properties of metal-polyphenol complexes, its anti-infective potential was investigated (Figure 5A). The photothermal properties of FVP@CCN were assessed, along with its antimicrobial efficacy against Gram-positive*S. aureus* and *MRSA*, Gram-negative*E. coli*. The hydrogel's photothermal performance was assessed under 808 nm NIR laser irradiation (Figure 5B). Under NIR irradiation at 1.0, 2.0, and 3.0 W/cm^2 for 10 min, the temperature of FVP@CCN$_{0.5}$ increased to 41.0, 54.8, and 72.6 °C, respectively (Figure 5C). Photothermal stability was assessed by monitoring the temperature changes during 10 min of laser irradiation, followed by a recovery to room temperature upon cessation of the laser (Figure S3). Notably, FVP@CCN hydrogel demonstrated highly reproducible photothermal capabilities, maintaining a consistent thermal response profile and the highest temperature without any attenuation and slightly increasing after consecutive cycles of near-infrared irradiation (2.0 W/cm^2) and natural cooling. The photothermal performance of different formulations of FVP@CCN was tested at a fixed power density of 2.0 W/cm^2. As depicted in Figure 5D, the temperature of the pure FVP group increased slightly to 33.2 °C due to the inherent black color. Interestingly, as the concentration of CCN increased, the temperature of each FVP@CCN group rose to varying extents. The FVP@CCN$_{0.1}$, containing the lowest CCN content, reached a temperature of 37.5 °C within 10 min, whereas the FVP@CCN$_1$ with the highest CCN content, achieved a temperature of 68.4 °C under the same conditions. These results confirm intrinsic photothermal properties of FVP. Furthermore, the phenolic hydroxyl group of CA present in CCN, as well as the coordination of phenolic hydroxyl-Cu^{2+}, may synergistically enhance the near-infrared absorption and photothermal conversion.

The antibacterial activity of various FVP@CCN hydrogels was evaluated using direct hydrogel-bacteria contact assays. As shown in Figures S4 (representative images) and 5E (quantitative analysis), all FVP@CCN formulations exhibited dose-dependent antibacterial effects without NIR irradiation. The antibacterial effects of the FVP group against the three types of bacterial strains were relatively weak. Upon the addition of CCN, the FVP@CCN$_{0.1}$ group, containing the lowest CCN content, resulted in survival rates of all three bacterial strains remaining below 60%. FVP@CCN$_{0.5}$ further reduced survival rates below 20%, while FVP@CCN$_1$ achieved >99.9% bacterial eradication.

The photothermal antibacterial effect of FVP@CCN was evaluated under NIR irradiation, and bacteria morphology was observed by SEM. The bacteria maintained a smooth and intact spherical or rod-shaped morphology for the control group (Figure 5F,H,J). In contrast, the bacteria of *S. aureus*, *E. coli*, and *MRSA* in the FVP and FVP + NIR groups displayed slight contractions and wrinkling. Interestingly, the bacterial cell membranes of *S. aureus*, *E. coli*, and *MRSA* in the FVP@CCN and FVP@CCN + NIR groups were significantly compromised, with cytoplasmic contents leaking out. FVP@CCN$_{0.5}$ with NIR irradiation reduced bacterial survival below 2%, significantly outperforming nonirradiated controls (Figure 5G,I,K). The impressive antibacterial performance of FVP@CCN$_{0.5}$ + NIR could be attributed to the combined effects of the bioactive components of FVP and CCN in the hydrogel, as well as the contributions of polyphenols and Cu^{2+} within the CCN, which collectively eradicate the majority of bacteria. Furthermore, the photothermal properties of FVP@CCN under NIR irradiation induce denaturation of certain enzymes and proteins within the bacteria at temperatures exceeding 50 °C, resulting in structural damage to the bacterial cells and achieving an antibacterial efficacy of over 98% (Figure 5A).

3.7. Biocompatibility of FVP@CCN Hydrogel.

In clinical scenarios involving wound dressings, hydrogels should exhibit excellent biocompatibility. The cytocompatibility of the FVP@CCN hydrogel was assessed with L929 fibroblasts via CCK-8 assay and Live/Dead staining. As shown in Figure 6A, with the exception of the FVP@CCN$_1$ group, which exhibited a cell viability of only 80%, all other groups demonstrated cell viability exceeding 100%, preliminarily indicating that the FVP@CCN series possesses good biocompatibility. Long-term cytotoxicity (1, 3, and 5 days) was assessed using cell Live/Dead staining and CCK-8. As illustrated in Figure 6B,C, L929 cells exhibited favorable conditions in all tested groups, with an increase in cell numbers. Except for the FVP@CCN$_1$ group, the cell numbers in other groups exceeded those in the control group. Interestingly, the cell proliferation rate of FVP@CCN$_{0.5}$ reached an impressive 350% on the fifth day, compared to 300% in the control group, which indicates that the FVP@CCN hydrogel loaded with a certain concentration range of CCN may promote cell proliferation.

Furthermore, the effectiveness of FVP@CCN in promoting the migration of fibroblasts (L929) *in vitro* was assessed using both the cell scratch assay and the transwell experiment. In the cell scratch assay (Figure 6D,E), compared to the cell migration rate for the control group of 45% at 24 h, both the FVP group and all FVP@CCN groups (except for FVP@CCN$_1$) significantly enhanced the migration of L929 cells, with migration rates all above 50% at 24 h. In the transwell migration experiment, except for the FVP@CCN$_1$ group, cell migration in the FVP group and other FVP@CCN groups was higher than that of the control group, with the FVP@CCN$_{0.2}$ group achieving an impressive cell migration rate of 140% (Figure 6F,G). Fibroblasts constitute one of the most essential cell types in the wound repair process, which participate directly in all stages of wound healing through biological behaviors such as proliferation, migration, differentiation, and synthesis of extracellular matrix components (e.g., collagen). These results of cell scratch assay and transwell assay using fibroblasts indicate that FVP@CCN containing CCN has good cytocompatibility and significantly promotes cell proliferation and migration, suggesting its potential application in wound healing.

The angiogenic potential of FVP@CCN hydrogel was evaluated through HUVEC tube formation assays. The FVP group showed minimal angiogenic improvement versus controls (Figure 6H,I). However, all FVP@CCN groups developed denser tubular networks, with FVP@CCN$_{0.5}$ forming the most extensive network after 6 h. This enhanced

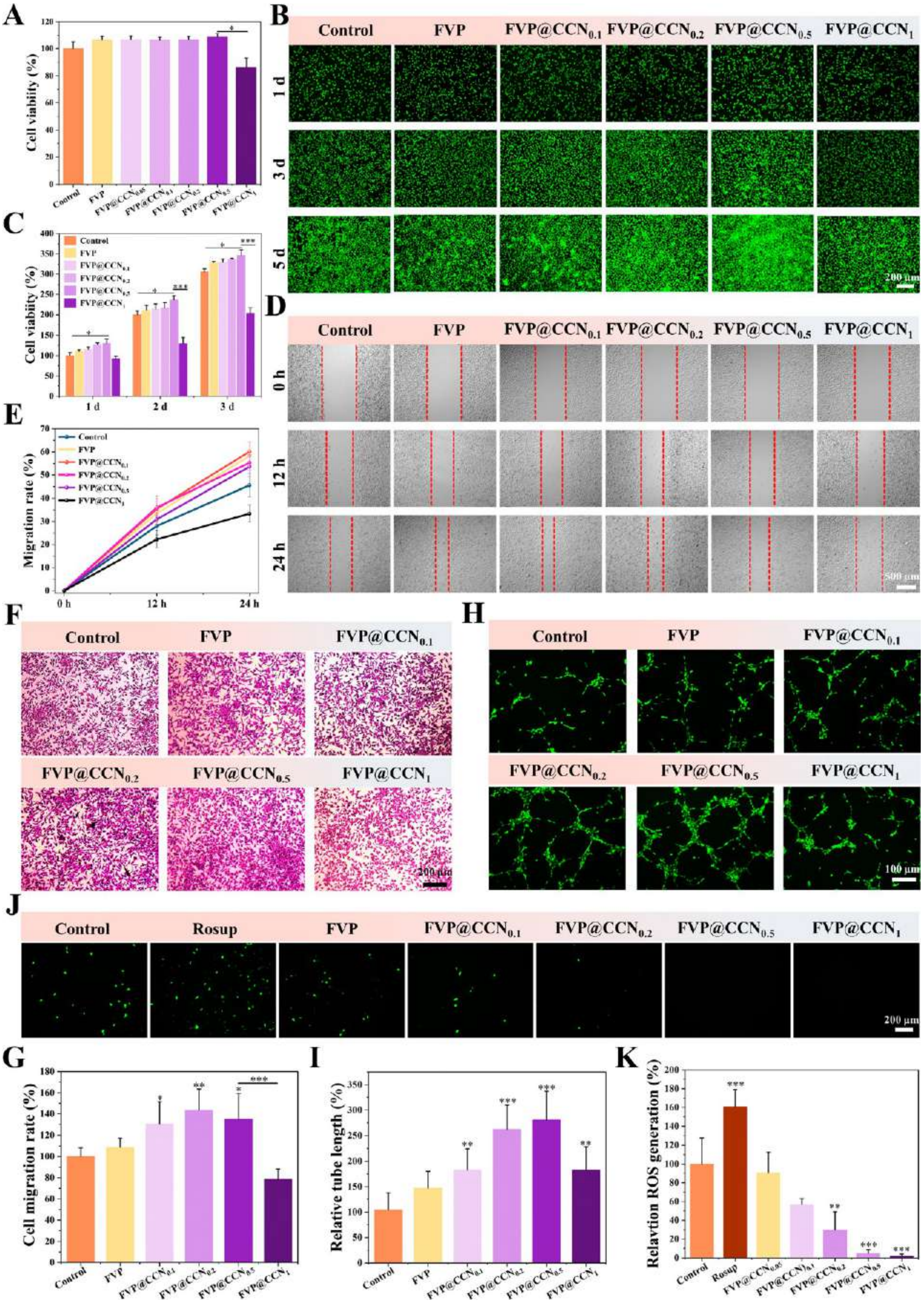

Figure 6. *In vitro* cytocompatibility, cell migration, angiogenic and cellular antioxidant properties of FVP@CCN hydrogels. (A) Cell cytotoxicity of FVP@CCN hydrogels against L929 for 24 h (n = 3). (B) Representative Live/Dead staining images and (C) corresponding quantitative cell viability of L929 after incubating with the extraction solution of FVP@CCN hydrogels for 1, 3, and 5 days (n = 3). (D) Scratch wound closure

Figure 6. continued

images and (E) quantitative cell migration rates ($n = 3$). (F) Transwell migration assay representative images and (G) quantitative migration rates. (H) Representative tube formation images and (I) relative tube lengths of HUVECs for 6 h ($n = 3$). (J) Fluorescence images and (K) relative fluorescence intensities obtained by ROS kit on L929 ($n = 3$). $^*p < 0.05$, $^{**}p < 0.01$, $^{***}p < 0.001$.

angiogenesis may be attributed to Cu^{2+}-mediated upregulation of angiogenic factors. The cellular antioxidant capacity of FVP@CCN was determined using the ROS assay kit, in which Rosup was employed to induce ROS overproduction in L929 cells, and 2,7-dichlorodihydrofluorescein diacetate (DCFH-DA) served as the probe to detect the amount of ROS generated within the cells. As shown in Figure 6J,K, the DCFH fluorescence intensity in cells treated with FVP@CCN hydrogel was significantly reduced compared to both the control and Rosup-treated groups. This decrease occurred in a concentration-dependent manner with respect to CCN. Notably, the FVP@CCN$_{0.5}$ group and the FVP@CCN$_1$ group showed almost no fluorescence signal, and their relative ROS generation content was below 5%, indicating that intracellular ROS were effectively scavenged. These findings highlight the distinctive antioxidant properties of the FVP@CCN hydrogel and suggest its potential effectiveness in the healing of diabetic wounds.

The FVP, caffeic acid, and Cu^{2+} in FVP@CCN can theoretically promote cell proliferation and migration,[71] while Cu^{2+} additionally enhances angiogenesis. Figure 4 confirms CCN's potent antioxidant activity.[72] However, FVP@CCN$_1$'s excessive CCN content reduced proliferation and migration compared with the controls and other formulation groups. Additionally, its ability to form tubular networks of HUVEC cells was inferior to that of the FVP@CCN$_{0.5}$ group, which contains less Cu^{2+}. The high concentration of CCN also signifies enhanced antioxidant capacity, which is why the cellular ROS levels in the FVP@CCN$_1$ group were not weaker than those observed in the other FVP@CCN groups. The FVP@CCN$_{0.5}$ group represents the optimal hydrogel ratio of FVP to CCN in the FVP@CCN hydrogel series in terms of cell compatibility and biological performance testing. Its exceptional biocompatibility, capacity to promote *in vitro* cell migration, angiogenic properties, and antioxidant characteristics collectively facilitate the overcoming of oxidative stress-induced barriers to angiogenesis in diabetic wounds, suggesting its potential to promote diabetic wound healing.

3.8. *In Vivo* Hemostatic Capacity of FVP@CCN Hydrogel.

Hemorrhage resulting from full-thickness skin defects presents an unavoidable challenge in clinical practice, highlighting the critical need for developing rapid hemostatic dressings to improve early wound management. The hemostatic performance of FVP@CCN hydrogel was systematically evaluated through two well-established bleeding models: tail amputation and liver incision models (Figure S5A). As shown in Figure S5A,B, the results demonstrate that FVP hydrogel significantly reduced blood loss at the transection site compared to the control group. Notably, FVP@CCN hydrogel nearly completely inhibited bleeding, showing statistically significant differences in blood loss comparing to that of the control group ($p < 0.05$). Consistent hemostatic effects were observed in the liver incision model (Figure S5A,C). These findings robustly demonstrate the exceptional hemostatic efficacy of FVP@CCN hydrogel *in vivo*, which might be attributed to the synergistic contributions of highly water-absorbable FVP hydrogel and the inclusion of polyphenol containing CCN.

3.9. *In Vivo* Diabetes Wound Regeneration Evaluation of FVP@CCN Hydrogel.

In vitro studies have demonstrated that FVP@CCN exhibits multiple therapeutic properties for diabetic wound treatment, including antimicrobial and antioxidant activities, promotion of cell proliferation and migration, and angiogenic stimulation. To further evaluate the therapeutic efficacy of FVP@CCN in treating diabetic wounds, we utilized streptozotocin (STZ) to induce male mice to form type 1 diabetes. Hyperglycemia levels exceeding 16.7 mM sustained for over 30 days were considered indicative of diabetic symptoms (Figure S6). As shown in Figure S7, healthy mice showed rounded pancreatic islets with normal architecture, where endocrine islets were clearly demarcated from exocrine acini, containing densely packed cells and minimal connective tissue. In contrast, the islets of diabetic mice failed to maintain a regular circular shape, demonstrating disorganized architecture. Furthermore, the pancreatic acini and islets showed intermingled growth, resulting in disrupted boundaries and blending with surrounding tissues, rendering them difficult to identify, which aligns with the typical characteristics of pancreatic changes in diabetic mice.[73,74] These findings confirm the establishment of a reliable diabetic animal model for subsequent wound healing studies (Figure 7A).

The full-thickness skin defect wound with an approximate diameter of 8 mm was generated on the dorsal region of these diabetic mice. Wounds were recorded and measured on days 0, 3, 7, and 14 post-treatment. As shown in Figure S8, thermal imaging analysis showed that the FVP@CCN hydrogel-treated group under NIR irradiation reached 55 °C within 10 min, which was consistent with the findings from *in vitro* experiments (Figure 5B). Figure 7B,C showed that FVP had a certain promoting effect on diabetic mouse wounds, while FVP@CCN exhibited impressive wound healing effects. As illustrated in Figure 7D, the wound size in the FVP@CCN and FVP@CCN + NIR groups significantly decreased on the third day. Interestingly, by the seventh day, the wound of the control group maintained a relatively large wound area, with a healing rate of only 51.85%, whereas the healing rate for the FVP@CCN group reached 80.00%, and the FVP@CCN + NIR group achieved as high as 91.11%, indicating near-complete healing of the FVP@CCN + NIR group. At 14 days, the control group still exhibited a substantial scar area, while the FVP@CCN + NIR group displayed minimal scarring and noticeable hair coverage, indicating superior healing quality.

To evaluate the healing effects of the FVP@CCN hydrogel from a histological perspective, regenerated skin tissue was collected for H&E staining and Masson's trichrome staining. As shown in Figure S9, inflammatory cell infiltration was observed in all groups after 3 days of treatment. However, the FVP, FVP@CCN, and FVP@CCN + NIR groups exhibited greater fibroblast migration and proliferation, with granulation tissue partially filling the wound area. After 7 days of treatment, the wound of control group still exhibited severe inflammation and inflammatory cell infiltration, with the epithelial tongue

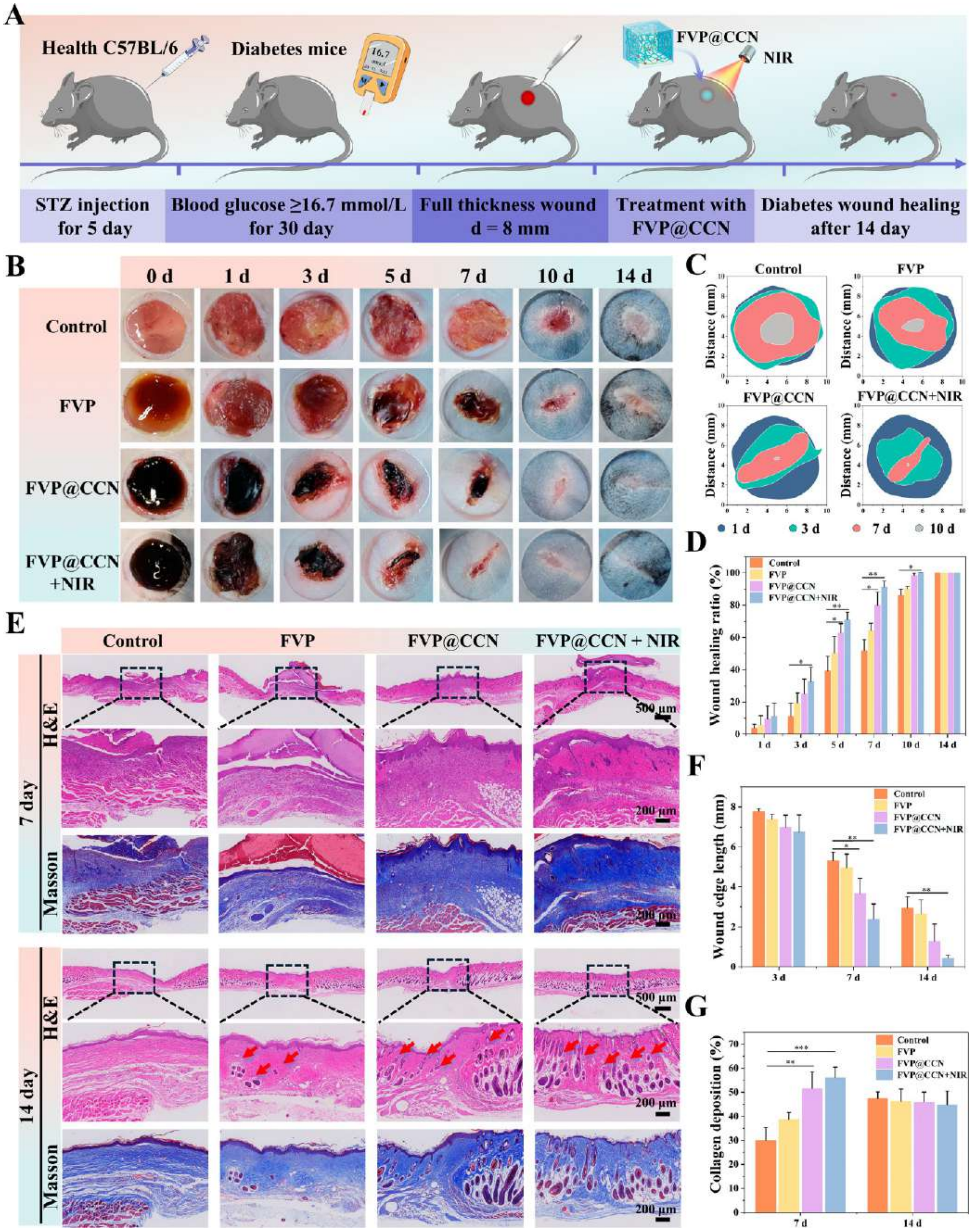

Figure 7. FVP@CCN Hydrogels accelerates the diabetic mice wound healing process. (A) The schematic illustration of establishment and treatment of diabetic mice wound model. (B) Representative photographs of wounds for the control, FVP hydrogel, FVP@CCN hydrogel and FVP@CCN + NIR groups at different time points. (C) Schematic illustration of wound and (D) the wound healing ratio ($n = 3$). (E) Representative H&E staining and Masson staining images on the 7th, and 14th day postsurgery (red arrows represent hair follicles, $n = 3$). (F) Wound edge length according to H&E images. (G) Collagen deposition ($n = 3$). $^*p < 0.05$, $^{**}p < 0.01$, $^{***}p < 0.001$.

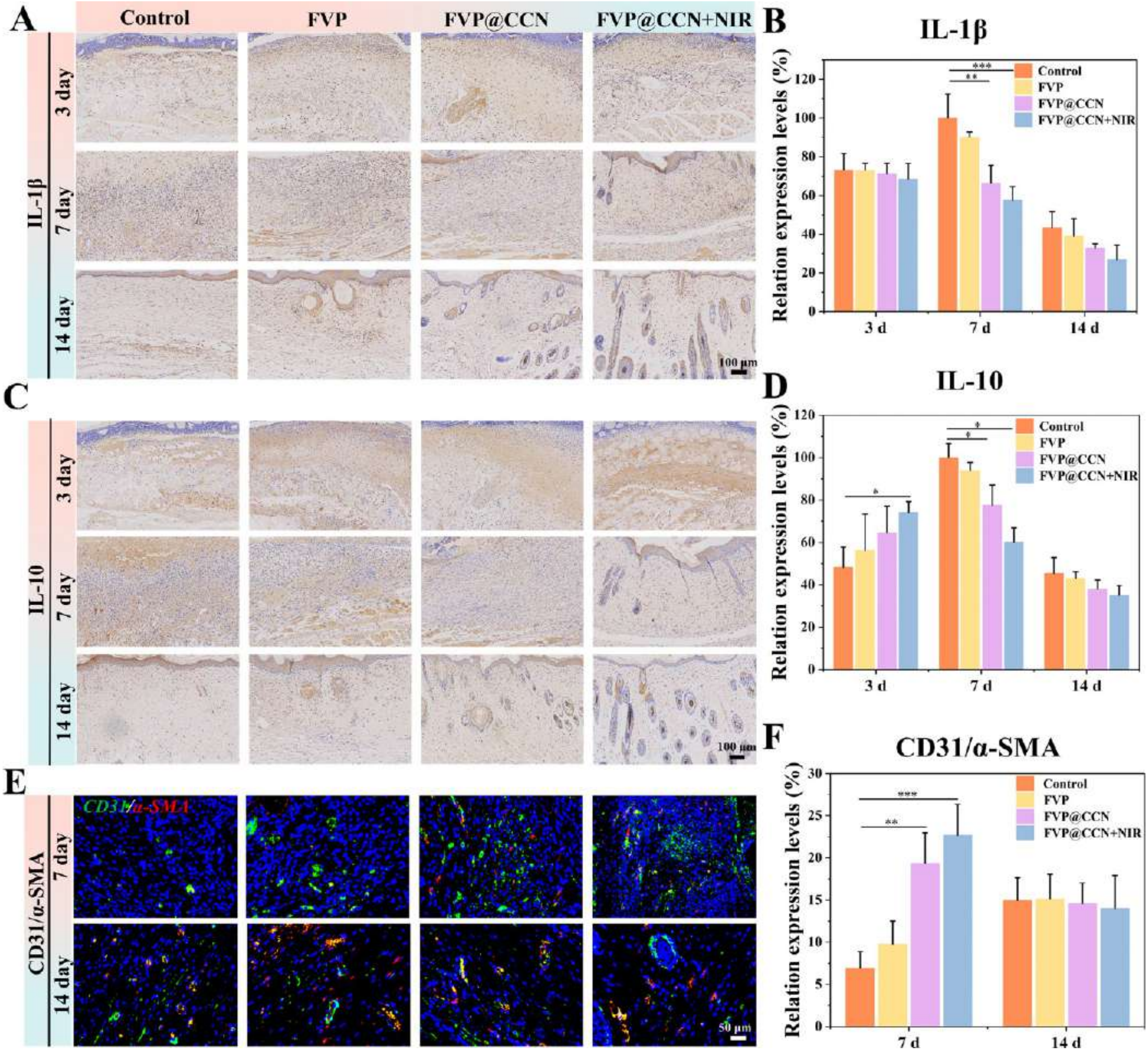

Figure 8. Immunohistochemical (IHC) and immunofluorescence (IF) staining evaluation of inflammation and angiogenesis. (A) Representative IHC staining images and (B) quantitative analysis of IL-1β expression levels on days 3, 7, and 14 ($n = 3$). (C) Representative IHC staining images and (D) quantitative analysis of IL-10 expression levels on days 3, 7, and 14 ($n = 3$). (E) Representative IF staining images and (F) quantitative analysis of CD31/α-SMA (green/red) expression on days 7 and 14 ($n = 3$). $^*p < 0.05$, $^{**}p < 0.01$, $^{***}p < 0.001$.

not yet migrating toward the center and the tissue structure being disordered (Figure 7E). In contrast, the FVP group developed complete dermal and epithelial tissues, although the wound width had not significantly narrowed (Figure 7F). Notably, compared to the control and FVP groups, the FVP@CCN and FVP@CCN + NIR groups achieved complete skin tissue, with an increased formation of capillaries. Most importantly, the regenerated skin tissue of the FVP@CCN + NIR group exhibited a dense arrangement of collagen fibers, with a collagen deposition ratio of 58.65% (Figure 7G). The dermis of the FVP@CCN + NIR group showed the formation of new skin appendages, such as hair follicles. At day 14, the healed skin tissues of the control and FVP groups exhibited a fully developed dermal layer. However, the regenerated skin tissues in the control group lacked skin appendages, whereas the FVP group's regenerated skin displayed a sparse presence of skin appendages along the periphery. Conversely, the wounds treated by FVP@CCN and FVP@CCN + NIR exhibited healing outcomes comparable to normal skin tissue. Particularly, the FVP@CCN + NIR group displayed advanced regeneration of skin structure with the most abundant hair follicle and sebaceous gland count (Figure S10), and the epidermal thickness matched that of the normal tissue. Additionally, the collagen deposition achieved homeostasis. These results demonstrated that FVP@CCN + NIR can effectively accelerate scarless wound healing in diabetic mice by promoting granulation tissue formation, facilitating epithelialization, enhancing the regeneration of skin appendages, and modulating collagen deposition and degradation.

3.10. Microenvironment Modulation and Angiogenesis Promotion by FVP@CCN Hydrogel for Accelerated Healing of Diabetic Wounds. Based on the promising wound healing outcomes observed in diabetic mice, we utilized immunohistochemical and immunofluorescence staining to conduct a further study to systematically investigate the anti-inflammatory and angiogenic effects of FVP@CCN hydrogel.

Oxidative stress activates multiple signaling pathways, resulting in the upregulation of chemokine and pro-inflammatory cytokine expression, thereby amplifying the inflammatory response, which is considered a major cause of prolonged healing time or even nonhealing of diabetic wounds.[1] Regenerated tissues were immunohistochemically stained for IL-1β and IL-10 (Figure 8A–D). By day 3, the expression levels of the pro-inflammatory cytokine IL-1β were comparable across all groups (Figure 8A,B). However, the FVP@CCN + NIR group exhibited a higher expression of the anti-inflammatory cytokine IL-10 (Figure 8C,D), suggesting that the hydrogel exerted a positive anti-inflammatory effect during the early stage of wound healing. By day 7, the expression levels of IL-1β and IL-10 in the FVP@CCN + NIR group both decreased. In contrast, the control group showed an increase in the expression of both, indicating a sustained inflammatory response in the control wounds. After 14 days of treatment, all four groups exhibited similar weak expressions of IL-1β and IL-10, but the control group had relatively higher expression levels than in the other three groups. These results indicated that FVP@CCN hydrogel treatment and NIR irradiation process diminish inflammatory stimuli, downregulate the inflammatory response, and facilitate a faster transition of the wound from the inflammatory phase to the proliferative phase, in which NIR irradiation further activates the photothermal antimicrobial activity of FVP@CCN, effectively eliminating bacterial infections and delivering localized thermotherapy that promotes tissue repair. In contrast, the wounds of the control group displayed prolonged inflammation, impairing repair rate and healing quality.

Neovascularization serves as a key indicator of skin tissue regeneration and functional restoration. Augmented neovascularization facilitates dermal reconstruction and promotes the reestablishment of intact cutaneous tissue.[25] Platelet endothelial cell adhesion molecule-1 (CD31), an endothelial cell junctional protein, serves as a specific marker for nascent vasculature, and alpha-smooth muscle actin (α-SMA) is a cytoskeletal protein that marks mature vascular structures. To determine the extent of neovascularization during the healing process, immunofluorescence analysis was conducted to detect the dynamic changes of CD31 and α-SMA during diabetic wound healing. As can be seen from Figure 8E,F, the expression levels of CD31 and α-SMA were markedly elevated in both the FVP@CCN and FVP@CCN + NIR groups relative to the control group at day 7 ($p < 0.01$). In addition, the effect was further enhanced by NIR irradiation in the FVP@CCN + NIR group. By day 14, the expression levels of CD31 and α-SMA in both FVP@CCN and FVP@CCN + NIR groups decreased, which may be attributed to the rapid wound healing with nearly all stages of wound healing completed. Physiological vascular regression occurred as neovascularization demand diminished. The comprehensive results indicated that the FVP@CCN hydrogels could promote the formation of neovasculature in diabetic wounds, thereby facilitating the delivery of increased oxygen, nutrients, and reparative cells to the wound site, which in turn accelerates the healing process. This may be attributed to the acidic microenvironment at the site of diabetic wounds, which induces the rapid release of Cu^{2+} and CA, and Cu^{2+} further promotes the formation of a large number of new vessels (Figure 3G). Additionally, on day 14, histological analysis of the heart, liver, spleen, lung, and kidney from diabetic mice was performed by H&E staining to evaluate potential *in vivo* toxicity. The results revealed no notable morphological alterations or pathological damage in the control group and FVP@CCN + NIR hydrogel group, indicating that the FVP@CCN hydrogel does not exhibit any apparent histopathological toxic effects (Figure S11).

3.11. *In Vivo* Antimicrobial Validation of FVP@CCN Hydrogels. The *in vivo* antibacterial performance of FVP@CCN hydrogels was systematically assessed using an infected diabetic mouse wound model. Observation of wounds (Figure S12A) on day 3 post-treatment revealed that the wounds of the control group exhibited persistent exudation with copious purulent discharge, indicating severe infection and healing impairment. While the FVP hydrogel group showed residual hydrogel coverage on the wound surface, the presence of purulent exudate at the wound base suggested limited antibacterial efficacy. In contrast, wounds treated with FVP@CCN hydrogel and FVP@CCN + NIR displayed dry surfaces without purulent discharge and demonstrated marked contraction, indicating a favorable healing progression. Quantitative bacterial culture analysis (Figure S12B,C) provided further confirmation: the control and FVP groups exhibited substantial bacterial proliferation, whereas the FVP@CCN group showed only 8.46% of the control's bacterial load ($p < 0.001$), with the FVP@CCN + NIR group achieving a remarkable reduction to 1.29% ($p < 0.001$). Microscopic examination of Gram-stained tissue sections revealed abundant clusters of Gram-positive cocci (purple) in the superficial necrotic tissue of the control and FVP groups (Figure S12D,E). The FVP@CCN group presented only scattered bacterial colonies, while the FVP@CCN + NIR group showed nearly undetectable bacterial colonization, with relative bacterial counts being reduced to merely 7.62% to that of the control group ($p < 0.001$). These consistent findings from both macroscopic and microscopic analytic results demonstrate that FVP@CCN hydrogel, particularly when combined with NIR therapy, effectively eliminates *S. aureus* colonization, controls infection, and promotes tissue repair in diabetic wounds.

The FVP@CCN hydrogel loaded with CCN can inhibit bacterial infection through its antibacterial and photothermal properties. The superior antioxidant capacity of CCN can scavenge excessive reactive oxygen species, balancing the oxidative/antioxidative stress in the wound, thereby modulating the inflammatory response. Concurrently, the affinity of FVP and catechol-containing caffeic acid for cellular and extracellular matrix proteins facilitates cell adhesion and migration. Cu^{2+} induces early stage angiogenesis, enhancing nutrient/oxygen delivery to support granulation tissue formation and re-epithelialization. Therefore, the FVP@CCN hydrogel may enhance the efficiency and quality of skin tissue repair by antimicrobial action, modulation of the inflammatory process, improvement of vascularization, promotion of collagen deposition and production of skin appendage glands, ultimately facilitating scarless healing of diabetic wounds (Scheme 1D).

4. CONCLUSIONS

In summary, we have developed a multifunctional polysaccharide hydrogel (FVP@CCN) derived from natural sources that is specifically tailored to meet the requirements for antimicrobial, antioxidant, anti-inflammatory, and pro-angiogenic properties in diabetic wound dressings. FVP@CCN hydrogels physically seal wounds in situ, providing environmental protection while exhibiting rapid degradation, pH-responsive release, and tunable mechanical properties. The incorporation of CCN endows the FVP@CCN hydrogels with photothermal properties and induces photothermal antibacterial activity *in vitro*. More importantly, FVP@CCN hydrogels demonstrated remarkable efficacy in reducing ROS levels, suppressing inflammation, facilitating angiogenesis, enhancing cell proliferation and migration, and exhibiting various other biological activities. Furthermore, *in vivo* assessment in diabetic mice substantiated the potent synergistic therapeutic efficacy of FVP@CCN for addressing multiple impediments to wound healing in diabetes. This hydrogel system intelligently and continuously modulated the wound microenvironment throughout various stages of healing by sequentially and continuously exerting antimicrobial, antioxidant, anti-inflammatory effects, promoting angiogenesis, stimulating cell proliferation, and facilitating hair follicle regeneration. Consequently, it significantly augmented the overall healing process of diabetic wounds. Overall, FVP@CCN hydrogels demonstrated significant application potential in complex wound/tissue healing scenarios characterized by physiological dysfunction, heightened susceptibility to bacterial infection, and adverse internal and external microenvironments.

■ ASSOCIATED CONTENT

Supporting Information

The Supporting Information is available free of charge at https://pubs.acs.org/doi/10.1021/acsami.5c11453.

> Experimental results including schematic diagram of synthesis of CCN, particle size of CCN, the temperature variation curve, the macroscopic photos of survival bacterial, hemostatic performance, diabetic mice blood glucose determination, H&E staining images of pancreas, the photothermal temperature change images of diabetic wounds, H&E staining and Masson staining images on the 3rd day postsurgery, number of hair follicles, biological safety, antibacterial efficacy *in vivo*, carbohydrate and protein content of the crude polysaccharides and FVP, chemical composition of FVP (PDF)

■ AUTHOR INFORMATION

Corresponding Authors

Wenzhen Liao − *Department of Nutrition and Food Hygiene, Guangdong Provincial Key Laboratory of Tropical Disease Research, School of Public Health, Southern Medical University, Guangzhou 510515, P. R. China;* orcid.org/0000-0002-5993-4276; Email: wenzhenliao@163.com

Jinshan Guo − *Department of Histology and Embryology, NMPA Key Laboratory for Safety Evaluation of Cosmetics, School of Basic Medical Sciences, Southern Medical University, Guangzhou 510515, P. R. China; CAS Key Laboratory of High-Performance Synthetic Rubber and Its Composite Materials, Changchun Institute of Applied Chemistry, Chinese Academy of Sciences, Changchun 130022, P. R. China;* orcid.org/0000-0001-8097-4902; Email: guojinshan@ciac.ac.cn, jsguo4127@163.com

Authors

Meimei Fu − *Department of Histology and Embryology, NMPA Key Laboratory for Safety Evaluation of Cosmetics, School of Basic Medical Sciences, Southern Medical University, Guangzhou 510515, P. R. China*

Qianru Xiang − *Department of Nutrition and Food Hygiene, Guangdong Provincial Key Laboratory of Tropical Disease Research, School of Public Health, Southern Medical University, Guangzhou 510515, P. R. China; Department of Clinical Nutrition, the Second School of Clinical Medicine, Zhujiang Hospital, Southern Medical University, Guangzhou 510280, China*

Zhuoyi Huang − *Department of Histology and Embryology, NMPA Key Laboratory for Safety Evaluation of Cosmetics, School of Basic Medical Sciences, Southern Medical University, Guangzhou 510515, P. R. China; CAS Key Laboratory of High-Performance Synthetic Rubber and Its Composite Materials, Changchun Institute of Applied Chemistry, Chinese Academy of Sciences, Changchun 130022, P. R. China*

Wenjun Luo − *Department of Histology and Embryology, NMPA Key Laboratory for Safety Evaluation of Cosmetics, School of Basic Medical Sciences, Southern Medical University, Guangzhou 510515, P. R. China*

Zhou Fang − *Department of Histology and Embryology, NMPA Key Laboratory for Safety Evaluation of Cosmetics, School of Basic Medical Sciences, Southern Medical University, Guangzhou 510515, P. R. China*

Jintao Li − *Department of Sports Medicine, Center for Orthopedic Surgery, Orthopedic Hospital of Guangdong Province, The Third School of Clinical Medicine, Guangdong Provincial Key Laboratory of Bone and Joint Degeneration Diseases, The Third Affiliated Hospital of Southern Medical University, Guangzhou 510630, P. R. China*

Yue Li − *Department of Plastic and Aesthetic Surgery, Nanfang Hospital of Southern Medical University, Guangzhou 510515, P. R. China*

Zijun Xia − *Department of Nutrition and Food Hygiene, Guangdong Provincial Key Laboratory of Tropical Disease Research, School of Public Health, Southern Medical University, Guangzhou 510515, P. R. China*

Yangjia Huang − *Department of Nutrition and Food Hygiene, Guangdong Provincial Key Laboratory of Tropical Disease Research, School of Public Health, Southern Medical University, Guangzhou 510515, P. R. China*

Yitao Zhao − *Department of Sports Medicine, Center for Orthopedic Surgery, Orthopedic Hospital of Guangdong Province, The Third School of Clinical Medicine, Guangdong Provincial Key Laboratory of Bone and Joint Degeneration Diseases, The Third Affiliated Hospital of Southern Medical University, Guangzhou 510630, P. R. China*

Complete contact information is available at: https://pubs.acs.org/10.1021/acsami.5c11453

Author Contributions

¶M.F., Q.X., and Z.H. contributed equally to this work. M.F.: conceptualization, writing—original draft, writing—review & editing, investigation, methodology, data curation. Q.X., Z.H.: conceptualization, writing—review & editing, investigation, methodology. W.L., Z.F., J.L., Y.L.: investigation, methodology, conceptualization and writing—original draft. Z.X., Y.H.: methodology, visualization and software. Y.Z.: writing—review & editing, methodology, formal analysis. W.L.: funding acquisition, supervision, conceptualization, resources. J.G.: funding acquisition, supervision, conceptualization, writing—review & editing, resources.

Notes

The authors declare no competing financial interest.

■ ACKNOWLEDGMENTS

This work was supported by the Natural Science Foundation of China (Grant Nos. 82272453 and U21A2099), the Youth Talent of Guangdong Special Support Program (Grant No. 0620220207), the Guangdong Basic and Applied Basic Research Foundation (Grant Nos. 2024A1515012664 and 2023A1515011065), the Guangdong Key R&D Program (Grant No. 2022B0202030001), and Tip-top Scientific and Technical Innovative Youth Talents of Guangdong Special Support Program (Grant No. 2021TQ06N130).

■ REFERENCES

(1) Qi, X.; Ge, X.; Chen, X.; Cai, E.; Xiang, Y.; Xu, H.; Li, Y.; Lan, Y.; Shi, Y.; Deng, H.; Shen, J. An Immunoregulation Hydrogel with Controlled Hyperthermia-Augmented Oxygenation and ROS Scavenging for Treating Diabetic Foot Ulcers. *Adv. Funct. Mater.* **2024**, *34* (33), 2400489.

(2) Zhang, Y.; Chen, Y.; Shao, P.; Luo, Y.; Liu, X.; Xu, T. Baicalin derivative dynamically cross-linked natural polysaccharide hydrogel for diabetic wound healing. *Chem. Eng. J.* **2024**, *497*, 154803.

(3) Zhang, G.; Samarawickrama, P. N.; Gui, L.; Ma, Y.; Cao, M.; Zhu, H.; Li, W.; Yang, H.; Li, K.; Yang, Y.; Zhu, E.; Li, W.; He, Y. Revolutionizing Diabetic Foot Ulcer Care: The Senotherapeutic Approach. *Aging Dis.* **2024**, *16*, 946.

(4) Popa, A. D.; Gavril, R. S.; Popa, I. V.; Mihalache, L.; Gherasim, A.; Nita, G.; Graur, M.; Arhire, L. I.; Nita, O. Survival Prediction in Diabetic Foot Ulcers: A Machine Learning Approach. *J. Clin. Med.* **2023**, *12* (18), 5816.

(5) Huang, J.; Yang, J.; Qi, H.; Xu, M.; Xu, X.; Zhu, Y. Prediction models for amputation after diabetic foot: systematic review and critical appraisal. *Diabetol. Metab. Syndr.* **2024**, *16* (1), 126.

(6) Shirzaei Sani, E.; Xu, C.; Wang, C.; Song, Y.; Min, J.; Tu, J.; Solomon, S. A.; Li, J.; Banks, J. L.; Armstrong, D. G.; Gao, W. A stretchable wireless wearable bioelectronic system for multiplexed monitoring and combination treatment of infected chronic wounds. *Sci. Adv.* **2023**, *9*, eadf7388.

(7) Cheng, C.; Zhong, H.; Zhang, Y.; Gao, X.; Wang, J.; Liu, J.; Han, X. Bacterial responsive hydrogels based on quaternized chitosan and GQDs-ε-PL for chemo-photothermal synergistic anti-infection in diabetic wounds. *Int. J. Biol. Macromol.* **2022**, *210*, 377−393.

(8) Mohsin, F.; Javaid, S.; Tariq, M.; Mustafa, M. Molecular immunological mechanisms of impaired wound healing in diabetic foot ulcers (DFU), current therapeutic strategies and future directions. *Int. Immunopharmacol.* **2024**, *139*, 112713.

(9) Duan, W.; Jin, X.; Zhao, Y.; Martin-Saldaña, S.; Li, S.; Qiao, L.; Shao, L.; Zhu, B.; Hu, S.; Li, F.; Feng, L.; Ma, Y.; Du, B.; Zhang, L.; Bu, Y. Engineering injectable hyaluronic acid-based adhesive hydrogels with anchored PRP to pattern the micro-environment to accelerate diabetic wound healing. *Carbohydr. Polym.* **2024**, *337*, 122146.

(10) Shao, Z.; Yin, T.; Jiang, J.; He, Y.; Xiang, T.; Zhou, S. Wound microenvironment self-adaptive hydrogel with efficient angiogenesis for promoting diabetic wound healing. *Bioact. Mater.* **2023**, *20*, 561−573.

(11) Huang, J.; Yang, R.; Jiao, J.; Li, Z.; Wang, P.; Liu, Y.; Li, S.; Chen, C.; Li, Z.; Qu, G.; Chen, K.; Wu, X.; Chi, B.; Ren, J. A click chemistry-mediated all-peptide cell printing hydrogel platform for diabetic wound healing. *Nat. Commun.* **2023**, *14* (1), 7856.

(12) Capó, X.; Monserrat-Mesquida, M.; Quetglas-Llabrés, M.; Batle, J. M.; Tur, J. A.; Pons, A.; Sureda, A.; Tejada, S. Hyperbaric Oxygen Therapy Reduces Oxidative Stress and Inflammation, and Increases Growth Factors Favouring the Healing Process of Diabetic Wounds. *Int. J. Mol. Sci.* **2023**, *24* (8), 7040.

(13) Deptuła, M.; Zawrzykraj, M.; Sawicka, J.; Banach-Kopeć, A.; Tylingo, R.; Pikuła, M. Application of 3D- printed hydrogels in wound healing and regenerative medicine. *Biomed. Pharmacother.* **2023**, *167*, 115416.

(14) Liao, Y.; Zhang, Z.; Zhao, Y.; Zhang, S.; Zha, K.; Ouyang, L.; Hu, W.; Zhou, W.; Sun, Y.; Liu, G. Glucose oxidase: An emerging multidimensional treatment option for diabetic wound healing. *Bioact. Mater.* **2025**, *44*, 131−151.

(15) Guo, Y.; Ding, S.; Shang, C.; Zhang, C.; Li, M.; Zhang, Q.; Gu, L.; Heng, B. C.; Zhang, S.; Mei, F.; Huang, Y.; Zhang, X.; Xu, M.; Jiang, J.; Guo, S.; Deng, X.; Chen, L. Multifunctional PtCuTe Nanosheets with Strong ROS Scavenging and ROS-Independent Antibacterial Properties Promote Diabetic Wound Healing. *Adv. Mater.* **2024**, *36* (8), e2306292.

(16) Yu, Z.; Li, M.; Yang, L.; Liu, H.; Ding, G.; Ma, S.; Liu, L.; Dong, S. Enhancing diabetic wound healing: A two-pronged approach with ROS scavenging and ROS-independent antibacterial properties. *Nano Today* **2024**, *57*, 102358.

(17) Monaghan, M. G.; Borah, R.; Thomsen, C.; Browne, S. Thou shall not heal: Overcoming the non-healing behaviour of diabetic foot ulcers by engineering the inflammatory microenvironment. *Adv. Drug Delivery Rev.* **2023**, *203*, 115120.

(18) Fu, M.; Zhao, Y.; Wang, Y.; Li, Y.; Wu, M.; Liu, Q.; Hou, Z.; Lu, Z.; Wu, K.; Guo, J. On-Demand Removable Self-Healing and pH-Responsive Europium-Releasing Adhesive Dressing Enables Inflammatory Microenvironment Modulation and Angiogenesis for Diabetic Wound Healing. *Small* **2022**, *19* (3), e2205489.

(19) Xiang, P.; Jiang, M.; Chen, X.; Chen, L.; Cheng, Y.; Luo, X.; Zhou, H.; Zheng, Y. Targeting Grancalcin Accelerates Wound Healing by Improving Angiogenesis in Diabetes. *Adv. Sci.* **2024**, *11* (14), e2305856.

(20) Rehak, L.; Giurato, L.; Meloni, M.; Panunzi, A.; Manti, G. M.; Uccioli, L. The Immune-Centric Revolution in the Diabetic Foot: Monocytes and Lymphocytes Role in Wound Healing and Tissue Regeneration-A Narrative Review. *J. Clin. Med.* **2022**, *11* (3), 889.

(21) Yuan, Y.; Fan, D.; Shen, S.; Ma, X. An M2 macrophage-polarized anti-inflammatory hydrogel combined with mild heat stimulation for regulating chronic inflammation and impaired angiogenesis of diabetic wounds. *Chem. Eng. J.* **2022**, *433*, 133859.

(22) Song, Y.; You, Y.; Xu, X.; Lu, J.; Huang, X.; Zhang, J.; Zhu, L.; Hu, J.; Wu, X.; Xu, X.; Tan, W.; Du, Y. Adipose-Derived Mesenchymal Stem Cell-Derived Exosomes Biopotentiated Extracellular Matrix Hydrogels Accelerate Diabetic Wound Healing and Skin Regeneration. *Adv. Sci.* **2023**, *10* (30), e2304023.

(23) Tu, C.; Lu, H.; Zhou, T.; Zhang, W.; Deng, L.; Cao, W.; Yang, Z.; Wang, Z.; Wu, X.; Ding, J.; Xu, F.; Gao, C. Promoting the healing of infected diabetic wound by an anti-bacterial and nano-enzyme-containing hydrogel with inflammation-suppressing, ROS-scavenging, oxygen and nitric oxide-generating properties. *Biomaterials* **2022**, *286*, 121597.

(24) Yadav, J. P.; Singh, A. K.; Grishina, M.; Pathak, P.; Verma, A.; Kumar, V.; Kumar, P.; Patel, D. K. Insights into the mechanisms of diabetic wounds: pathophysiology, molecular targets, and treatment strategies through conventional and alternative therapies. *Inflammopharmacology* **2024**, *32* (1), 149−228.

(25) Wu, Y.; Wang, Y.; Zheng, C.; Hu, C.; Yang, L.; Kong, Q.; Zhang, H.; Wang, Y. A Versatile Glycopeptide Hydrogel Promotes Chronic Refractory Wound Healing Through Bacterial Elimination, Sustained Oxygenation, Immunoregulation, and Neovascularization. *Adv. Funct. Mater.* **2023**, *33* (49), 2305992.

https://doi.org/10.1021/acsami.5c11453
ACS Appl. Mater. Interfaces 2025, 17, 53145−53167

(26) Xu, Z.; Liu, G.; Huang, J.; Wu, J. Novel Glucose-Responsive Antioxidant Hybrid Hydrogel for Enhanced Diabetic Wound Repair. *ACS Appl. Mater. Interfaces* **2022**, *14* (6), 7680−7689.

(27) Liang, Y.; He, J.; Guo, B. Functional Hydrogels as Wound Dressing to Enhance Wound Healing. *ACS Nano* **2021**, *15* (8), 12687−12722.

(28) Brumberg, V.; Astrelina, T.; Malivanova, T.; Samoilov, A. Modern Wound Dressings: Hydrogel Dressings. *Biomedicines* **2021**, *9* (9), 1235.

(29) Maleki, A.; He, J.; Bochani, S.; Nosrati, V.; Shahbazi, M.-A.; Guo, B. Multifunctional Photoactive Hydrogels for Wound Healing Acceleration. *ACS Nano* **2021**, *15* (12), 18895−18930.

(30) Huang, S.; Hong, X.; Zhao, M.; Liu, N.; Liu, H.; Zhao, J.; Shao, L.; Xue, W.; Zhang, H.; Zhu, P.; Guo, R. Nanocomposite hydrogels for biomedical applications. *Bioeng. Transl. Med.* **2022**, *7* (3), e10315.

(31) Wan, J.; Liang, Y.; Wei, X.; Liang, H.; Chen, X. L. Chitosan-based double network hydrogel loading herbal small molecule for accelerating wound healing. *Int. J. Biol. Macromol.* **2023**, *246*, 125610.

(32) Ju, Y.; Hu, Y.; Yang, P.; Xie, X.; Fang, B. Extracellular vesicle-loaded hydrogels for tissue repair and regeneration. *Mater. Today Bio* **2023**, *18*, 100522.

(33) Wells, A.; Nuschke, A.; Yates, C. C. Skin tissue repair: Matrix microenvironmental influences. *Matrix Biol.* **2016**, *49*, 25−36.

(34) El-Husseiny, H. M.; Mady, E. A.; Hamabe, L.; Abugomaa, A.; Shimada, K.; Yoshida, T.; Tanaka, T.; Yokoi, A.; Elbadawy, M.; Tanaka, R. Smart/stimuli-responsive hydrogels: Cutting-edge platforms for tissue engineering and other biomedical applications. *Mater. Today Bio* **2022**, *13*, 100186.

(35) Wu, Y.; Wang, Y.; Long, L.; Hu, C.; Kong, Q.; Wang, Y. A spatiotemporal release platform based on pH/ROS stimuli-responsive hydrogel in wound repairing. *J. Controlled Release* **2022**, *341*, 147−165.

(36) Jia, X.; Dou, Z.; Zhang, Y.; Li, F.; Xing, B.; Hu, Z.; Li, X.; Liu, Z.; Yang, W.; Liu, Z. Smart Responsive and Controlled-Release Hydrogels for Chronic Wound Treatment. *Pharmaceutics* **2023**, *15* (12), 2735.

(37) Jin, S.; Newton, M. A. A.; Cheng, H.; Zhang, Q.; Gao, W.; Zheng, Y.; Lu, Z.; Dai, Z.; Zhu, J. Progress of Hydrogel Dressings with Wound Monitoring and Treatment Functions. *Gels* **2023**, *9* (9), 694.

(38) Berradi, A.; Aziz, F.; Achaby, M. E.; Ouazzani, N.; Mandi, L. A Comprehensive Review of Polysaccharide-Based Hydrogels as Promising Biomaterials. *Polymers* **2023**, *15* (13), 2908.

(39) Zhu, T.; Mao, J.; Cheng, Y.; Liu, H.; Lv, L.; Ge, M.; Li, S.; Huang, J.; Chen, Z.; Li, H.; Yang, L.; Lai, Y. Recent Progress of Polysaccharide-Based Hydrogel Interfaces for Wound Healing and Tissue Engineering. *Adv. Mater. Interfaces* **2019**, *6* (17), 1900761.

(40) Benalaya, I.; Alves, G.; Lopes, J.; Silva, L. R. A Review of Natural Polysaccharides: Sources, Characteristics, Properties, Food, and Pharmaceutical Applications. *Int. J. Mol. Sci.* **2024**, *25* (2), 1322.

(41) Mohanty, S.; Swarup, J.; Priya, S.; Jain, R.; Singhvi, G. Exploring the potential of polysaccharide-based hybrid hydrogel systems for their biomedical and therapeutic applications: A review. *Int. J. Biol. Macromol.* **2024**, *256*, 128348.

(42) Ma, S.; Zhang, H.; Xu, J. Characterization, Antioxidant and Anti-Inflammation Capacities of Fermented Flammulina velutipes Polyphenols. *Molecules* **2021**, *26* (20), 6205.

(43) Ma, S.; Xu, J.; Lai, T.; Xu, W.; Zhang, J.; Zhang, H.; Zhang, W. Inhibitory Effect of Fermented Flammulina velutipes Polysaccharides on Mice Intestinal Inflammation. *Front. Nutr.* **2022**, *9*, 934073.

(44) Chen, F.; Zhang, Q.; Wu, P.; Zhao, Y.; Suo, X.; Xiao, A.; Ke, M.; He, X.; Tong, Z.; Chen, Y. Green fabrication of seedbed-like Flammulina velutipes polysaccharides-derived scaffolds accelerating full-thickness skin wound healing accompanied by hair follicle regeneration. *Int. J. Biol. Macromol.* **2021**, *167*, 117−129.

(45) Zhu, Y.; Chen, F.; Wu, M.; Xiang, J.; Yan, F.; Xie, Y.; Tong, Z.; Chen, Y.; Cai, L. Biocompatible and antibacterial Flammulina velutipes-based natural hybrid cryogel to treat noncompressible hemorrhages and skin defects. *Front. Bioeng. Biotechnol.* **2022**, *10*, 960407.

(46) Xiong, M.; Yang, X.; Shi, Z.; Xiang, J.; Gao, H.; Ji, S.; Li, Y.; Pi, W.; Chen, H.; Zhang, H.; Wang, M.; Li, Y.; Hong, Y.; Liu, D.; Fu, X.; Dong, Y.; Sun, X. Programmable Artificial Skins Accomplish Antiscar Healing with Multiple Appendage Regeneration. *Adv. Mater.* **2024**, *36*, 2407322.

(47) Li, J.; Ke, H.; Lei, X.; Zhang, J.; Wen, Z.; Xiao, Z.; Chen, H.; Yao, J.; Wang, X.; Wei, Z.; Zhang, H.; Pan, W.; Shao, Y.; Zhao, Y.; Xie, D.; Zeng, C. Controlled-release hydrogel loaded with magnesium-based nanoflowers synergize immunomodulation and cartilage regeneration in tendon-bone healing. *Bioact. Mater.* **2024**, *36*, 62−82.

(48) Wang, Y.; Zhao, Y.; Ma, S.; Fu, M.; Wu, M.; Li, J.; Wu, K.; Zhuang, X.; Lu, Z.; Guo, J. Injective Programmable Proanthocyanidin-Coordinated Zinc-Based Composite Hydrogel for Infected Bone Repair. *Adv. Healthcare Mater.* **2024**, *13* (6), e2302690.

(49) Fu, M.; Zhao, Y.; Wang, Y.; Li, Y.; Wu, M.; Liu, Q.; Hou, Z.; Lu, Z.; Wu, K.; Guo, J. On-Demand Removable Self-Healing and pH-Responsive Europium-Releasing Adhesive Dressing Enables Inflammatory Microenvironment Modulation and Angiogenesis for Diabetic Wound Healing. *Small* **2023**, *19* (3), e2205489.

(50) Hao, Y.; Liao, X.; Wang, X.; Lao, S.; Liao, W. The biological regulatory activities of Flammulina velutipes polysaccharide in mice intestinal microbiota, immune repertoire and heart transcriptome. *Int. J. Biol. Macromol.* **2021**, *185*, 582−591.

(51) Wu, M.; Zhao, Y.; Tao, M.; Fu, M.; Wang, Y.; Liu, Q.; Lu, Z.; Guo, J. Malate-Based Biodegradable Scaffolds Activate Cellular Energetic Metabolism for Accelerated Wound Healing. *ACS Appl. Mater. Interfaces* **2023**, *15* (44), 50836−50853.

(52) Li, Y.; Miao, Y.; Yang, L.; Wang, G.; Fu, M.; Wang, Y.; Fu, D.; Huang, J.; Wang, J.; Fan, Z.; Lu, Z.; Guo, J.; Hu, Z. Malate-based polyester chemically shielded metal-phenolic networks coated artificial hair fibers with long-lasting antimicrobial and anti-inflammatory performance. *Chem. Eng. J.* **2023**, *455*, 140572.

(53) Wang, H.; Song, F.; Feng, J.; Qi, X.; Ma, L.; Xie, L.; Shi, W.; Zhou, Q. Tannin coordinated nanozyme composite-based hybrid hydrogel eye drops for prophylactic treatment of multidrug-resistant Pseudomonas aeruginosa keratitis. *J. Nanobiotechnol.* **2022**, *20* (1), 445.

(54) Wu, K.; Wu, X.; Guo, J.; Jiao, Y.; Zhou, C. Facile Polyphenol-Europium Assembly Enabled Functional Poly(l-Lactic Acid) Nanofiber Mats with Enhanced Antioxidation and Angiogenesis for Accelerated Wound Healing. *Adv. Healthcare Mater.* **2021**, *10* (19), 2100793.

(55) Teng, M.; Li, Z.; Wu, X.; Zhang, Z.; Lu, Z.; Wu, K.; Guo, J. Development of tannin-bridged cerium oxide microcubes-chitosan cryogel as a multifunctional wound dressing. *Colloids Surf., B* **2022**, *214*, 112479.

(56) Shao, N.; Huang, S.; Huang, Y.; Pan, M.; Xie, Y.; Chen, Q.; Chen, C.; Pan, J.; Zhou, Y. Smart Enzyme-Like Polyphenol-Copper Spray for Enhanced Bacteria-Infected Diabetic Wound Healing. *Small* **2024**, *20* (22), 2308295.

(57) Chen, C.; Lin, M.; Wahl, C.; Li, Y.; Zhou, W.; Wang, Z.; Zhang, Y.; Mirkin, C. A. Dynamic Metal-Phenolic Coordination Complexes for Versatile Surface Nanopatterning. *J. Am. Chem. Soc.* **2023**, *145* (14), 7974−7982.

(58) Lin, S.; Cheng, Y.; Zhang, H.; Wang, X.; Zhang, Y.; Zhang, Y.; Miao, L.; Zhao, X.; Wei, H. Copper Tannic Acid Coordination Nanosheet: A Potent Nanozyme for Scavenging ROS from Cigarette Smoke. *Small* **2020**, *16* (27), 1902123.

(59) Wen, M.; Wang, T.; Li, N.; Wu, Y.; Zhang, L.; Xue, Y.; Shang, L. Polyphenol-Copper Derived Self-Cascade Nanozyme Hydrogel in Boosting Oxygenation and Robust Revascularization for Tissue Regeneration. *Adv. Funct. Mater.* **2024**, *34* (40), 2403634.

(60) Pang, L.; Tian, P.; Cui, X.; Wu, X.; Zhao, X.; Wang, H.; Wang, D.; Pan, H. In Situ Photo-Cross-Linking Hydrogel Accelerates Diabetic Wound Healing through Restored Hypoxia-Inducible Factor 1-Alpha Pathway and Regulated Inflammation. *ACS Appl. Mater. Interfaces* **2021**, *13* (25), 29363−29379.

(61) Hossain Rakin, R.; Kumar, H.; Rajeev, A.; Natale, G.; Menard, F.; Li, I. T. S.; Kim, K. Tunable metacrylated hyaluronic acid-based hybrid bioinks for stereolithography 3D bioprinting. *Biofabrication* **2021**, *13* (4), 044109.

(62) Yang, J.; Yang, K.; Man, W.; Zheng, J.; Cao, Z.; Yang, C. Y.; Kim, K.; Yang, S.; Hou, Z.; Wang, G.; Wang, X. 3D bio-printed living nerve-like fibers refine the ecological niche for long-distance spinal cord injury regeneration. *Bioact. Mater.* **2023**, *25*, 160−175.

(63) Enrique Cuevas-Suárez, C.; Aldrighi Münchow, E.; Gonçalves Schwarzbold, C.; Kuhn Rutz, J.; Fernandes da Silva, A.; Piva, E. Effect of naturally derived antioxidants as polymerization inhibitors on experimental adhesive resins. *J. Photochem. Photobiol., A* **2023**, *436*, 114368.

(64) He, Y.; Li, N.; Xiang, Z.; Rong, Y.; Zhu, L.; Huang, X. Natural polyphenol as radical inhibitors used for DLP-based 3D printing of photosensitive gels. *Mater. Today Commun.* **2022**, *33*, 104698.

(65) Geng, H.; Zhong, Q. Z.; Li, J.; Lin, Z.; Cui, J.; Caruso, F.; Hao, J. Metal Ion-Directed Functional Metal-Phenolic Materials. *Chem. Rev.* **2022**, *122* (13), 11432−11473.

(66) Xie, L.; Li, J.; Wang, L.; Dai, Y. Engineering metal-phenolic networks for enhancing cancer therapy by tumor microenvironment modulation. *Wiley Interdiscip. Rev.: Nanomed. Nanobiotechnol.* **2023**, *15* (3), e1864.

(67) Zeng, H.; Li, D.; He, Q.; Zheng, X.; Chen, X.; Jian, G.; Zhang, H.; Chen, T. A microenvironment responsive nanoparticle regulating osteoclast fate to promote bone repair in osteomyelitis. *Mater. Today Bio* **2025**, *32*, 101777.

(68) Norioka, C.; Inamoto, Y.; Hajime, C.; Kawamura, A.; Miyata, T. A universal method to easily design tough and stretchable hydrogels. *NPG Asia Mater.* **2021**, *13* (1), 34.

(69) Xiong, Y.; Chu, X.; Yu, T.; Knoedler, S.; Schroeter, A.; Lu, L.; Zha, K.; Lin, Z.; Jiang, D.; Rinkevich, Y.; Panayi, A. C.; Mi, B.; Liu, G.; Zhao, Y. Reactive Oxygen Species-Scavenging Nanosystems in the Treatment of Diabetic Wounds. *Adv. Healthcare Mater.* **2023**, *12* (25), e2300779.

(70) Yu, R.; Zhang, H.; Guo, B. Conductive Biomaterials as Bioactive Wound Dressing for Wound Healing and Skin Tissue Engineering. *Nano-Micro Lett.* **2021**, *14* (1), 1.

(71) Seo, S. H.; Lee, S.-H.; Cha, P.-H.; Kim, M.-Y.; Min, D. S.; Choi, K.-Y. *Polygonum aviculare* L. and its active compounds, quercitrin hydrate, caffeic acid, and rutin, activate the Wnt/β-catenin pathway and induce cutaneous wound healing. *Phytother. Res.* **2016**, *30* (5), 848−854.

(72) Wen, M.; Wang, T.; Li, N.; Wu, Y.; Zhang, L.; Xue, Y.; Shang, L. Polyphenol-Copper Derived Self-Cascade Nanozyme Hydrogel in Boosting Oxygenation and Robust Revascularization for Tissue Regeneration. *Adv. Funct. Mater.* **2024**, *34*, 2403634.

(73) Kotb El-Sayed, M. I.; Al-Massarani, S.; El Gamal, A.; El-Shaibany, A.; Al-Mahbashi, H. M. Mechanism of antidiabetic effects of Plicosepalus Acaciae flower in streptozotocin-induced type 2 diabetic rats, as complementary and alternative therapy. *BMC Complementary Med. Ther.* **2020**, *20* (1), 290.

(74) Sheweita, S. A.; Mashaly, S.; Newairy, A. A.; Abdou, H. M.; Eweda, S. M. Changes in Oxidative Stress and Antioxidant Enzyme Activities in Streptozotocin-Induced Diabetes Mellitus in Rats: Role of Alhagi maurorum Extracts. *Oxid. Med. Cell. Longevity* **2016**, *2016*, 5264064.